A Two-Level Time-Stepping Method for Layered Ocean Circulation Models: Further Development and Testing

Robert L. Higdon
Department of Mathematics
Oregon State University
Corvallis, Oregon 97331-4605

This article was published in *Journal of Computational Physics*, vol. 206, pp. 463–504, 2005, and is posted with permission from Elsevier.

Abstract

In [10] a two-level time-stepping method was developed for layered ocean circulation models. The method is designed to be used with a barotropic-baroclinic splitting that separates the fast and slow motions into subsystems that are solved by different techniques. The discussion in [10] includes the development of the scheme, a linearized stability analysis, a description of some techniques for practical implementation in a nonlinear model, and some numerical testing. Subsequent additional testing revealed a need for further development of the techniques for nonlinear implementation. The purpose of the present paper is to describe these algorithmic improvements and to develop and report some additional numerical experiments. The algorithmic issues involve the relation between velocity and momentum density as layer thicknesses tend to zero, limiting mass and momentum fluxes between thick and thin cells near variable bottom topography, solving the barotropic equations that describe the fast motions in the system, and conserving mass within individual layers. This paper also develops a test problem involving external and internal Rossby waves in a two-layer fluid; the separation into modes makes it possible to test the time-stepping schemes for the barotropic and baroclinic systems independently. The paper concludes with some numerical tests that include the Rossby wave problem, an upwelling/downwelling problem that involves fluid interfaces moving upward and downward along sloping bottom topography, and a double-gyre circulation that displays meanders and eddies.

Key words: timestepping, barotropic-baroclinic splitting, layered ocean circulation models

AMS subject classifications: 65M12, 86A05

1 Introduction

A time-stepping method for layered ocean circulation models was developed in [10]. The method was designed for usage with a barotropic-baroclinic splitting, in which the fast and slow motions in the system are approximately separated into subproblems that are solved by different techniques. The method involves two time levels in order to avoid the sawtooth computational mode allowed by the three-level leapfrog method, which has traditionally been used in geophysical fluid dynamics, and in order to facilitate the usage of advection algorithms for mass and momentum. In a linearized stability analysis given in [10], the method was shown to be stable and essentially nondissipative. Some numerical tests of the method were given in [10], along with some preliminary ideas for practical implementation in nonlinear models. These latter ideas were described in Section 4 of [10].

Further testing of this time-stepping scheme and associated algorithms revealed a need for further development of the implementation procedures discussed in Section 4 of [10]. The purpose of the present paper is to document these new developments and to describe some of the recent numerical tests.

In the terminology used here, a "layered" ocean model is one in which the vertical coordinate is density, potential density (density adjusted adiabatically to a reference pressure), or some other related quantity. For a given fluid parcel, such a quantity is approximately constant in time, except perhaps in the vertically-homogeneous mixed layer at the top of the ocean. In a setting of this nature, surfaces of constant vertical coordinate are approximately material surfaces, and a vertical discretization amounts to dividing the fluid into material layers having distinct physical properties. Subtle exchanges between layers are then under the control of the modeler, and this can be important in situations such as long-term climate simulations. Models with this type of vertical coordinate are also known as "isopycnic" models.

Section 2 of the present paper summarizes the governing equations and time-stepping method used here. Section 3 describes the algorithmic developments, which can be summarized as follows.

(1) Thin layers. In order to use a (nearly) nonoscillatory advection algorithm for momentum, the momentum equation is written in a flux form with momentum density (velocity times layer thickness) as the dependent variable. However, it is then necessary to extract an advective velocity which can be used in the flux terms. If one simply divides momentum density by layer thickness, the results can be erratic when the thickness tends to zero, so we describe a method for suppressing such behavior. This method has implications for implementing the Coriolis terms, which are also discussed here.

(2) Bottom topography. Interfaces between layers can intersect the bottom of the fluid domain, which in general can have varying elevation. At such locations a layer can have widely varying thicknesses at adjacent grid points or cells. One issue encountered in recent experiments is the possible transport of unrealistically large amounts of mass or momentum from a thick cell to an adjacent thin cell, and this can generate highly irregular behavior in the computed solution. We describe a method for limiting the fluxes of mass and momentum in such situations.

(3) Solution of the barotropic (fast) equations. An alternating-direction implicit (ADI) method for solving this system was described in [10], and it was used successfully in some computations that involved integrating to an analytical steady state. However, in a recent test involving external Rossby waves for which the time dependence is known essentially exactly, the ADI method gave results that are highly inaccurate. Accordingly, an alternate scheme is mentioned here, along with a discussion of some implementation issues.

(4) Conservation of mass. An equation for layer thickness in the baroclinic (slow) subsystem given by Bleck and Smith [3] does not yield exact conservation of mass in individual layers. An alternate approach is described here which does yield such conservation. This approach is related to ideas used by Hallberg [8] and more recently by Bentsen and by Dukowicz (personal communications).

Section 4 develops a test problem involving Rossby waves. These are waves for which the restoring mechanism is based on vorticity instead of gravity, and they play an important role in the development of large-scale circulation systems. The present test problem involves linearized motions in a two-layer fluid in a straight channel and a linearly-varying Coriolis parameter. This problem admits both gravity waves and Rossby waves, and within each category it admits both external waves and internal waves. A simple test involving gravity waves was given in [10], so the present emphasis is on Rossby waves. The time dependences of modal solutions of this system can be determined exactly, up to the numerical accuracy in computing the eigenvalues and eigenvectors of certain matrices that arise during the development of this problem. In the barotropic-baroclinic splitting used here, the barotropic subsystem mainly represents the relatively fast external motions, and the baroclinic subsystem mainly represents the remaining (slow) motions. The external and internal modes in the present test problem make it possible to evaluate the time-stepping in the two subsystems separately.

Section 5 describes the results of some numerical computations involving the algorithms described here. The first set of computations is based on the Rossby wave test problem developed in Section 4. The second set involves a two-layer fluid with variable bottom topography, for which the interface between the layers intersects the sloping bottom. Due to

the action of wind stress at the top of the fluid, the lower layer wells upward to the surface in some regions, and the interface moves upward and downward along the bottom topography. For large t, the solutions closely match analytical steady-state solutions. The last set of computations involves a double-gyre circulation in a two-layer fluid in a rectangular domain having a level bottom. The fluid is forced by a sinusoidally-varying wind stress. In this case the lower layer wells up to the surface in part of the domain, and the flow displays many meanders and eddies but no numerical grid noise.

2 Governing equations and time-stepping method

The present section summarizes the systems of partial differential equations to be considered here, along with the time-stepping method developed in [10].

2.1 Governing equations

In the following, it is assumed that the fluid is in hydrostatic balance, which is equivalent to the "shallow-water" assumption that the depth of the fluid is small compared to the horizontal dimensions of the phenomena being modeled. Consider a vertically-discrete system consisting of R layers of constant density, and number the layers 1 through R, with the indices increasing downward. Let α_r denote the specific volume (reciprocal of density) in layer r, $\mathbf{u}_r(x,y,t) = (u_r(x,y,t), v_r(x,y,t))$ denote the horizontal velocity in layer r, $\Delta p_r(x,y,t)$ denote the vertical pressure difference between the bottom and top of layer r, and $M_r(x,y,t) = \alpha p + gz$ denote the Montgomery potential in layer r. Here, g is the acceleration due to gravity. The hydrostatic condition $\partial p/\partial z = -\alpha^{-1} g$ implies that the Montgomery potential is independent of depth in a layer of constant density. Also let $\nabla = (\partial/\partial x, \partial/\partial y)$, $p_r(x,y,t)$ denote the pressure at the bottom of layer r, f denote the Coriolis parameter, and $\mathbf{u}_r^\perp = (-v_r, u_r)$. We then consider the "primitive equation" system

$$\frac{\partial \mathbf{u}_r}{\partial t} + (\mathbf{u}_r \cdot \nabla)\,\mathbf{u}_r + f\mathbf{u}_r^\perp = -\nabla M_r + \frac{g\Delta\tau_r}{\Delta p_r} + \frac{1}{\Delta p_r}\nabla\cdot(A_H \Delta p_r \nabla \mathbf{u}_r) \tag{1}$$

$$\frac{\partial \Delta p_r}{\partial t} + \nabla\cdot(\mathbf{u}_r \Delta p_r) = 0 \tag{2}$$

$$M_{r+1} - M_r = p_r(\alpha_{r+1} - \alpha_r) \tag{3}$$

(Bleck and Smith [3]).

This system can be regarded as a stack of single-layer shallow-water models, with a means of communicating pressure effects between layers. The hydrostatic assumption implies that the pressure increment Δp_r is the weight per unit horizontal area in layer r, so the quantity $\mathbf{u}_r \Delta p_r$ in (2) is g times the horizontal mass flux in that layer. The quantity Δp_r will also be

regarded as the "thickness" of layer r. In the mass conservation equation (2) it is assumed that there is no transport of mass between layers, for the sake of simplicity. However, in a realistic ocean model it is possible for such transports to take place, as noted in Section 3.4.

In the second term on the right side of (1), the quantity $\Delta\tau_r$ is a vertical difference of lateral stresses acting on the top and bottom of layer r. These stresses are due to wind stress at the top of the fluid domain, frictional stress at the bottom, and interior shear stress due to vertical variations of the horizontal velocity. The last term on the right side of (1) represents the effect of horizontal viscosity. For most of the computations described in Section 5, this term will be set to zero.

2.2 Barotropic-baroclinic splitting

In solutions of the system (1)–(3), the most rapid motions are external gravity waves. Here, "external" means that all layers thicken or thin by approximately the same proportion at any given time and horizontal position, so the behavior of the mass field can be detected from the motions of the free surface at the top of the fluid. With external motions, the velocity field is very nearly independent of depth. External gravity waves can be up to two orders of magnitude faster than other motions such as currents and internal waves, so for the sake of computational efficiency it is advisable to model the external motions with a two-dimensional subsystem (the "barotropic" subsystem). Such a system is obtained by a vertical averaging and/or summation of (1)–(2). This system also captures external Rossby waves, which are discussed in Section 4 and which travel more slowly than the external gravity waves. The dynamics of external waves are similar to those that would be found if one were to neglect the density variations in the ocean and then model the ocean with the shallow-water equations for a single layer.

The remaining motions in the ocean include advective motions and internal waves. The latter are manifested by motions of layer interfaces within the fluid. These relatively slow motions are fully three-dimensional, and they can be modeled by a three-dimensional subsystem (the "baroclinic" subsystem).

The baroclinic subsystem can be solved with an explicit time discretization and a time increment Δt that is appropriate for resolving the slow motions. The two-dimensional barotropic subsystem can either be solved implicitly with the same Δt or explicitly with many short substeps. In the following, we use a barotropic-baroclinic splitting introduced by Bleck and Smith [3], with modifications developed by Higdon and de Szoeke [11] in order to improve its stability.

Let $p'_b(x, y)$ be the pressure at the bottom of the fluid domain at a reference state, such as an equilibrium state or initial state, and let $p_b(x, y, t)$ be the bottom pressure at an arbitrary

state. Define a dimensionless quantity $\eta(x,y,t)$ by $p_b = p'_b + p'_b\eta = (1+\eta)p'_b$, so that η is the relative perturbation in bottom pressure, with $|\eta| \ll 1$. The perturbation $p'_b\eta$ in bottom pressure will serve as the mass variable in the barotropic subsystem. A baroclinic mass variable $\Delta p'_r$ can then be defined by $\Delta p_r(x,y,t) = (1+\eta(x,y,t))\Delta p'_r(x,y,t)$ for $1 \le r \le R$. This relation is based on the idea that an external wave causes all fluid layers to thicken or thin by approximately the same proportion. It then follows that $\sum_{r=1}^{R} \Delta p'_r = p'_b$. Also define the mass-weighted vertical average

$$\bar{\mathbf{u}}(x,y,t) \;=\; \sum_{r=1}^{R} \frac{\Delta p_r}{p_b}\mathbf{u}_r \;=\; \sum_{r=1}^{R} \frac{\Delta p'_r}{p'_b}\mathbf{u}_r, \tag{4}$$

which will serve as a barotropic velocity. (The second equation in (4) uses the relations $\Delta p_r = (1+\eta)\Delta p'_r$ and $p_b = (1+\eta)p'_b$.) A baroclinic velocity is then defined by $\mathbf{u}'_r(x,y,t) = \mathbf{u}_r(x,y,t) - \bar{\mathbf{u}}(x,y,t)$, so that $\mathbf{u}_r = \bar{\mathbf{u}} + \mathbf{u}'_r$. A comparison with (4) shows that $\mathbf{u}'$ has mass-weighted vertical average equal to zero.

A vertical average of the momentum equation (1) and a vertical sum of the mass equation (2) yield the barotropic equations

$$\frac{\partial \bar{\mathbf{u}}}{\partial t} + f\bar{\mathbf{u}}^{\perp} \;=\; -\,\overline{\nabla M} + \mathbf{G} \tag{5}$$

$$\frac{\partial}{\partial t}(p'_b\eta) + \nabla\cdot(p'_b\bar{\mathbf{u}}) \;=\; 0, \tag{6}$$

where $\bar{\mathbf{u}}^{\perp} = (-\bar{v}, \bar{u})$. In (5) the quantity $\overline{\nabla M}$ is the mass-weighted vertical average of ∇M; an explicit representation of this term is given by Higdon [9]. The quantity $\mathbf{G}(x,y,t)$ is a residual term that includes the vertical average of the nonlinear, stress, and viscosity terms in (1). An implementation of $\mathbf{G}$ is indicated in Section 2.3.

The derivation of (6) includes an assumption that the pressure is constant at the top of the fluid, and the divergence term uses the approximation $\nabla\cdot(p_b\bar{\mathbf{u}}) \approx \nabla\cdot(p'_b\bar{\mathbf{u}})$, as $p_b = (1+\eta)p'_b$ with $|\eta| \ll 1$. The quantity $p'_b\eta$ is equal to g times the perturbation in the mass per unit horizontal area in the water column, and the quantity $p'_b\bar{\mathbf{u}}$ is equal to g times the lateral mass flux over the depth of the fluid.

A manipulation of the layer thickness equation (2) given by Bleck and Smith [3] yields

$$\frac{\partial \Delta p'_r}{\partial t} + \nabla\cdot(\mathbf{u}_r\Delta p'_r) \;=\; \frac{\Delta p'_r}{p'_b}\nabla\cdot(p'_b\bar{\mathbf{u}}). \tag{7}$$

However, this equation is not in conservation form, and numerical experiments have shown that the amount of mass in individual layers can vary slightly with time, even though equation (2) implies that the total mass in each layer is constant. If needed, exact conservation (up to roundoff error) can be obtained with a method described in Section 3.4. That method

employs the full thickness equation (2) instead of (7) by enforcing a kind of compatibility between (2) and the barotropic mass equation (6) at each baroclinic step.

A baroclinic momentum equation can be obtained by subtracting the barotropic equation (5) from (1) to yield an equation for $\mathbf{u}'_r$. An alternative, used in [10], is to combine such an equation with the baroclinic thickness equation (7) to yield equations for the quantities $u'_r\Delta p'_r$ and $v'_r\Delta p'_r$. Since Δp_r is g times the mass per unit horizontal area in layer r, these quantities can be regarded as components of baroclinic momentum per unit horizontal area (times g). The equation for $u'_r\Delta p'_r$ is

$$\begin{aligned}
&\frac{\partial}{\partial t}\left(u'_r\Delta p'_r\right) + \frac{\partial}{\partial x}\Big[u_r\left(u'_r\Delta p'_r\right)\Big] + \frac{\partial}{\partial y}\Big[v_r\left(u'_r\Delta p'_r\right)\Big] \\
&\quad = \quad fv'_r\Delta p'_r - \Delta p'_r\left(\frac{\partial M_r}{\partial x} - (\overline{\nabla M})_x\right) + g(\Delta\tau_r)_x + \nabla\cdot(A_H\Delta p'_r\nabla u_r) - G_x\Delta p'_r \\
&\quad - \quad u_r\Delta p'_r\frac{\partial\bar{u}}{\partial x} - v_r\Delta p'_r\frac{\partial\bar{u}}{\partial y} + \frac{u'_r\Delta p'_r}{p'_b}\nabla\cdot(p'_b\bar{\mathbf{u}}),
\end{aligned} \tag{8}$$

and the equation for $v'_r\Delta p'_r$ (not stated explicitly in [10]) is

$$\begin{aligned}
&\frac{\partial}{\partial t}\left(v'_r\Delta p'_r\right) + \frac{\partial}{\partial x}\Big[u_r\left(v'_r\Delta p'_r\right)\Big] + \frac{\partial}{\partial y}\Big[v_r\left(v'_r\Delta p'_r\right)\Big] \\
&\quad = \quad -fu'_r\Delta p'_r - \Delta p'_r\left(\frac{\partial M_r}{\partial y} - (\overline{\nabla M})_y\right) + g(\Delta\tau_r)_y + \nabla\cdot(A_H\Delta p'_r\nabla v_r) - G_y\Delta p'_r \\
&\quad - \quad u_r\Delta p'_r\frac{\partial\bar{v}}{\partial x} - v_r\Delta p'_r\frac{\partial\bar{v}}{\partial y} + \frac{v'_r\Delta p'_r}{p'_b}\nabla\cdot(p'_b\bar{\mathbf{u}}).
\end{aligned} \tag{9}$$

The left sides of (8) and (9) are in flux form, which facilitates the usage of a (nearly) nonoscillatory advection scheme for those terms. As described in [10], the terms on the right side can be regarded as forcing terms that are implemented with a Strang [18] splitting. The condition that the mass-weighted vertical average of baroclinic velocity is zero is equivalent to the zero-sum condition

$$\sum_{r=1}^{R} u'_r\Delta p'_r = \sum_{r=1}^{R} v'_r\Delta p'_r = 0 \tag{10}$$

for baroclinic momentum.

In a numerical test involving a linear external Rossby wave described in Section 5.1, the magnitude of the barotropic velocity is typically about three orders of magnitude larger than the baroclinic velocity. In a similar test involving an internal Rossby wave, the magnitude of the baroclinic velocity is typically about one to two orders of magnitude larger than the barotropic velocity. Although the above splitting is not exact, these experiments suggest that the splitting is nearly exact, in the linear case.

2.3 Time-stepping method

This subsection summarizes the time-stepping method of [10] and associated algorithms, as modified by the developments described in Section 3 of the present paper. In the following, it is assumed that the solution is known at time t_n and that the solution is being computed at time $t_{n+1} = t_n + \Delta t$, where the time increment Δt is appropriate for stably resolving the slow motions in the system.

1. Predict the baroclinic velocity $\mathbf{u}'_r = (u'_r, v'_r)$ at time t_{n+1}. To do this, use the momentum equations (8)–(9) and baroclinic mass equation (7), with upwind approximations to the flux terms and with the forcing terms evaluated at time t_n. Use the procedure in Section 3.1 to extract u'_r and v'_r. The quantities G_x and G_y in (8) and (9) are computed by enforcing the zero-sum condition (10) on $u'_r \Delta p'_r$ and $v'_r \Delta p'_r$, in a manner similar to the one described in Section 2.3 of Higdon and de Szoeke [11].

2. Predict the barotropic variables $\bar{u}$, $\bar{v}$, and $p'_b \eta$ by solving the barotropic system (5)–(6). The quantity $\overline{\nabla M}$ in (5) involves both the barotropic quantity $p'_b \eta$ and the baroclinic mass variables $\Delta p'_r$. (See Higdon [9].) During the present step, use the values of $\Delta p'_r$ from time t_n and the value of $\mathbf{G} = (G_x, G_y)$ computed in Step 1.

3. Apply a (nearly) nonoscillatory advection scheme to the thickness equation (2), together with the procedures described in Section 3.4, to compute Δp_r at time t_{n+1}. The procedures of Section 3.4 guarantee conservation of mass in each layer. For an advective velocity $\mathbf{u}_r$, use a value at time $t_{n+1/2} = t_n + \Delta t/2$ obtained by adding the average of the old and predicted baroclinic velocities in layer r to the time average of the barotropic velocities computed from time t_n to time t_{n+1} during Step 2 above. For the sake of computing forcing terms at time t_{n+1}, extract $\Delta p'_r = \Delta p_r/(1+\eta)$ by using the predicted value of η.

4. Correct the baroclinic velocity $\mathbf{u}'_r = (u'_r, v'_r)$ by applying an advection scheme to the momentum equations (8)–(9). In the pressure and viscous terms and in the advective velocity, use time averages of baroclinic and barotropic quantities analogous to those used in Step 3. In the Coriolis terms, use unweighted averages of baroclinic velocities at times t_n and t_{n+1}. The Coriolis terms are thus implicit, and if values of u and v are defined at different spatial locations then these terms can be implemented with an iteration. (For the computations described in Section 5, four iterations are used.)

5. Correct the barotropic variables $\bar{u}$, $\bar{v}$, and $p'_b \eta$. For the baroclinic quantities appearing in $\overline{\nabla M}$, use averages of values from times t_n and t_{n+1}. Repeat the flux adjustment

described in Section 3.4, so as to ensure compatibility between the final values of Δp_r and $p_b' \eta$.

For large-scale motions, the dominant balance in the momentum equation is typically the "geostrophic balance" between the Coriolis terms and the pressure gradient. Because of the time averaging used in Step 4, these terms are both evaluated at the intermediate time $t_{n+1/2}$ during the correction step. If they were evaluated at different times, then there would be a first-order error in the geostrophic balance.

Smolarkiewicz and Margolin [17] point out that a second-order advection algorithm requires that the advective velocity be evaluated at time $t_{n+1/2}$, so that certain error terms are compensated appropriately. Such an advective velocity is provided by the above scheme. The advection method used in the numerical computations described in Section 5 is the multidimensional positive definite advection transport algorithm (MPDATA), which is described in [17]. With this method, solutions that are initially nonnegative remain nonnegative in the absence of forcing. This is an essential property when the layer thickness equation (2) is solved in situations when the thicknesses can tend to zero. In the computations described in Section 5, MPDATA is also used to solve the momentum equations. For that case MPDATA is adapted to handle fields of varying sign by using the first of two options described in Section 3.2(4) of [17]. MPDATA involves an upwind step followed by antidiffusive corrections, and for the computations described in Section 5 two antidiffusive corrections are used.

3 Algorithmic developments

This section describes several developments related to the practical implementation of the two-level time-stepping method outlined in Section 2.3. These include matters related to thin layers and Coriolis terms, bottom topography, the solution of the barotropic equations, and conservation of mass. All of these algorithmic ideas are incorporated into the numerical computations reported in Section 5.

For definiteness, it is assumed here that the system is discretized in space on a staggered "C-grid". This grid is used, for example, in the Miami Isopycnic Coordinate Ocean Model and in the Hybrid Coordinate Ocean Model (Bleck [2]). With this grid, values of u are defined at the centers of the edges of mass cells corresponding to minimal and maximal x, and values of v are defined at the centers of the edges corresponding to minimal and maximal y. Portions of the discussion in Section 3.1 are specific to the C-grid, but the ideas in the remainder of Section 3 can be applied more generally.

3.1 Thin layers and Coriolis terms

In the implementation of the two-level method as described in Section 2, the dependent variables in the baroclinic momentum equations are chosen to be the momentum densities $u'_r \Delta p'_r$ and $v'_r \Delta p'_r$ in order that the equations can be written in flux form for usage with a (nearly) nonoscillatory advection method. However, at each baroclinic time step the velocities u'_r and v'_r must be extracted from the momentum densities in order to obtain advective velocities $u_r = \bar{u} + u'_r$ and $v_r = \bar{v} + v'_r$ that can be used when computing fluxes of mass and momentum. The present subsection describes a procedure for doing this on a C-grid which is simpler and more robust than the one described in Section 4.3 of [10]. This procedure has implications for the implementation of the Coriolis terms, and this matter is discussed here as well.

For definiteness, consider the extraction of u'_r from $u'_r \Delta p'_r$. Both of these quantities are defined at u-points. In order to obtain u'_r at any such point, one could simply divide $u'_r \Delta p'_r$ by a value of $\Delta p'_r$ at that u-point, which will be denoted here by $(\Delta p'_r)^u$. However, the value of $(\Delta p'_r)^u$ must be obtained from some kind of interpolation between the values of $\Delta p'_r$ at adjacent mass points, and this interpolated value is affected by interpolation error and by numerical errors in the values being interpolated. As $(\Delta p'_r)^u \rightarrow 0$, these errors can cause erratic behavior in the values of u'_r that are extracted, in the sense that $|u'_r|$ can exceed physically realistic bounds at various locations. These erratic values can then cause a violation of the Courant-Friedrichs-Lewy stability condition.

Section 4.3 of [10] described a method for controlling the erratic behavior by limiting the mass fluxes that are generated by the extracted velocities. Schär and Smolarkiewicz [16] had earlier developed a different procedure for extracting velocity from momentum density. In their analysis the momentum and mass variables are defined at the same points, and they limited antidiffusive corrections to mass and momentum fluxes so that the ratio of momentum density and layer thickness is bounded.

In order to describe the present extraction process in greater detail, consider the extraction of velocity during the correction step for the two-level method; the case of the prediction step is analogous but simpler. At a certain stage, the algorithm has produced a provisional value for $u' \Delta p'$ in layer r at time t_{n+1}, based on the effects of the nonlinear terms, forcing terms such as $\overline{\nabla M}$, and the average of the Coriolis term based on velocity at time t_n and the Coriolis term based on the predicted velocity at time t_{n+1}. The next step is to introduce the effects of shear stresses between layers (i.e., vertical viscosity). These effects represent a vertical diffusion of velocity, not momentum, so the values of velocity must enter the computation explicitly at this stage. The result of this step is velocity instead of momentum density. As noted in Section 4.4 of [10], if $(\Delta p'_r)^u \rightarrow 0$ the effect of the shear stress is to

cause u'_r to tend to the average of the values of u' in the layers immediately above and/or below layer r. This regularizing effect then suppresses erratic behavior in the velocity field in thin layers.

In [10] the momentum densities $u'_r\Delta p'_r$ and $v'_r\Delta p'_r$ are then reconstructed with a multiplication. In the u-equation, the Coriolis term $fv'_r\Delta p'_r$ is iterated so that the value of this term is based on the final value of $v'_r\Delta p'_r$ at time t_{n+1} instead of the predicted value. Due to the staggered nature of the C-grid, the value of $v'_r\Delta p'_r$ at a u-point was taken to be a simple four-point average of $v'_r\Delta p'_r$ at the four nearest v-points. The iteration of Coriolis terms modifies the momentum density $u'_r\Delta p'_r$, and it could lead to substantial changes in the corresponding value of u'_r; for example, this could happen if the thickness $\Delta p'_r$ at one of the neighboring v-points is many times greater than the thickness at the u-point in question. At locations where the layer thickness tends to zero, the relative variation in $\Delta p'_r$ between consecutive grid points can be substantial and actually unbounded, and the corresponding effect on velocity can also be unbounded. The implementation of the Coriolis terms in momentum form thus compromises the regularizing effect of the shear stress, and it is then necessary to adopt an extraction procedure which limits velocity, such as the one described in Section 4.3 of [10].

However, the following alternative is simpler, and experiments suggest that it is also more reliable. When the shear stress has been implemented, the result of that step is velocity instead of momentum density, and the velocities in thin layers are typically well-behaved in the sense of lying between physically realistic bounds. At this stage, simply keep the problem in terms of velocity for a while longer, before the final values of momentum are obtained by multiplying by values of $\Delta p'_r$ at velocity points. That is, the Coriolis terms are implemented with a fixed-point iteration of the implicit equations

$$\begin{aligned} u_r'^{\,n+1} &= (u'_r)^* + \frac{f\Delta t}{2}(v_r'^{\,n+1} - v_r'^{\,pred}) \\ v_r'^{\,n+1} &= (v'_r)^* - \frac{f\Delta t}{2}(u_r'^{\,n+1} - u_r'^{\,pred}), \end{aligned} \tag{11}$$

where $u_r'^{\,pred}$ and $v_r'^{\,pred}$ are values of u' and v' produced during the prediction step, and $(u'_r)^*$ and $(v'_r)^*$ represent the results of the implementation of shear stress during the present correction step. The division by 2 on the right sides of (11) is due to the averaging of data from times t_n and t_{n+1}, and the former has already been incorporated into $(u'_r)^*$ and $(v'_r)^*$. Also, values of $(u'_r)^*$ and $(v'_r)^*$ include Coriolis terms at time t_{n+1} based on predicted velocity, and the quantities on the right side of (11) represent corrections to such terms. On a C-grid, the values of u'_r and v'_r are defined at different spatial locations, so the terms involving f on the right side of (11) involve some spatial averages.

For example, consider the u-point located at position $(x_{i-1/2}, y_j)$ between the mass cells with centers at (x_{i-1}, y_j) and (x_i, y_j). The four v-points that are closest to u-point $(x_{i-1/2}, y_j)$ are then $(x_i, y_{j\pm1/2})$ and $(x_{i-1}, y_{j\pm1/2})$. The Coriolis term fv at the u-point $(x_{i-1/2}, y_j)$ could then be represented with the unweighted average of v at the four neighbors. An alternative is a mass-weighted average described by Sadourny [15] in the context of the shallow-water equations for a single-layer fluid. Sadourny showed that if the shallow-water system is discretized in space on a C-grid, with t remaining continuous, then the total energy in the system is unaffected by the Coriolis terms if the following averaging scheme is used to implement those terms. At the v-point $(x_i, y_{j-1/2})$, define a two-point sum of thicknesses by $S_{i,j-1/2} = \Delta p'_{i,j} + \Delta p'_{i,j-1}$. At the point $(x_{i-1/2}, y_{j-1/2})$, which lies on a corner of four mass cells, a value of fv can be defined by the mass-weighted average

$$(fv)_{i-1/2,j-1/2} = f_{i-1/2,j-1/2} \left[\frac{S_{i,j-1/2}}{S_{i,j-1/2} + S_{i-1,j-1/2}} v_{i,j-1/2} + \frac{S_{i-1,j-1/2}}{S_{i,j-1/2} + S_{i-1,j-1/2}} v_{i-1,j-1/2} \right],$$

which involves the thicknesses at those four neighboring cells. A value of fv at the u-point $(x_{i-1/2}, y_j)$ is then given by

$$(fv)_{i-1/2,j} = \frac{1}{2} \left[(fv)_{i-1/2,j-1/2} + (fv)_{i-1/2,j+1/2} \right]. \tag{12}$$

If the Coriolis terms are discretized either with unweighted averages or with the Sadourny energy-conserving scheme (12), then the value of $|fv|$ at a u-point does not exceed $|f|$ times the maximum value of $|v|$ found at the four neighbors. Such an approach, combined with the regularization provided by the implementation of shear stress, suppresses erratic behavior in the velocity field in a multi-layer model. After the implementation of Coriolis terms produces values of u'_r and v'_r, the final values of momentum density are obtained by multiplying by values of $\Delta p'_r$ at u-points and v-points, respectively.

If a model is run without an implementation of shear stress between layers, and if layer thicknesses can tend to zero with the configuration being used, then the following procedure can be used to suppress erratic velocities. If the thickness of the layer drops below a prescribed threshold (e.g., a fraction of a meter), then require that the velocity in a given layer must be the average of the values in the layers immediately above and/or below. If the thickness is above a larger threshold (e.g., twice the preceding), then impose no such requirement. If the thickness is between the two thresholds, then use a linear transition between these two cases. This process can be implemented by solving a linear system in the vertical dimension, at each horizontal location. Once this regularization is performed, the Coriolis terms can be implemented as above.

3.2 Bottom topography

The present subsection describes a procedure for limiting mass and momentum fluxes near variable bottom topography. In the absence of such a limiter, thin cells can experience inputs of mass or momentum which are physically unrealistic and which can generate irregular behavior and violations of the Courant-Friedrichs-Lewy condition.

The issue of variable bottom topography was also discussed in Section 4.5 of [10]. In that discussion the main issue was the computation of the layer thickness $\Delta p'_r$ at velocity points on a C-grid. For definiteness, consider such a computation at a u-point. The procedure in [10] yields a positive value of the interpolated thickness $(\Delta p'_r)^u$ if and only if a centered difference approximation to $\partial M_r/\partial x$ is considered to have physical significance, according to criteria described in [10]. At locations where layer interfaces intersect bottom topography it is possible for such numerical approximations to be meaningless in terms of the dynamics of the fluid, and the goal is to prevent such cases from affecting the computed solution. As $(\Delta p'_r)^u \to 0$ the momentum equation is considered to lose its physical significance, but in that case the velocity u'_r tends to the average of the velocities in the layers that are immediately above and/or below. In effect, the momentum equation in layer r is disregarded in such situations, as desired.

In the interpolation scheme described in [10], the bottom topography is regarded as piecewise constant, with the constants representing averages in mass cells. The idea of piecewise constant ("stairstep") topography will also be used here to discuss a different issue, which is related to fluxes of mass and momentum.

Figure 1(a) illustrates this issue for the case of mass flux. In this figure the horizontal axis is the x-axis, and variations with respect to y are not illustrated. At the location of mass cell A, the bottom topography is much lower than at mass cell B. The boxed region in mass cell A (including the shaded subregion at the top) represents the mass in a given layer r in that cell, and the boxed region in cell B represents the mass in the same layer, but in cell B. However, in cell B layer r is much thinner than in cell A.

Now consider the possible transfer of mass between the two cells in layer r. For the sake of simplicity, suppose that the upwind method is used as the advection scheme. In that case, the mass flux at a cell edge is the velocity at the edge times the layer thickness in the upstream direction, i.e., in the cell that is being drained. Suppose that this advective velocity u_r is negative, and suppose that the magnitude of u_r would cause some portion, say 10%, of the fluid in cell B to move into cell A in one time step. This transfer of mass has a very small effect on cell A. However, suppose $u_r > 0$ and that 10% of the mass in cell A would move into cell B. This would have a very large effect on cell B, and it could involve lifting some mass up over the bottom topography. One can question whether a transfer

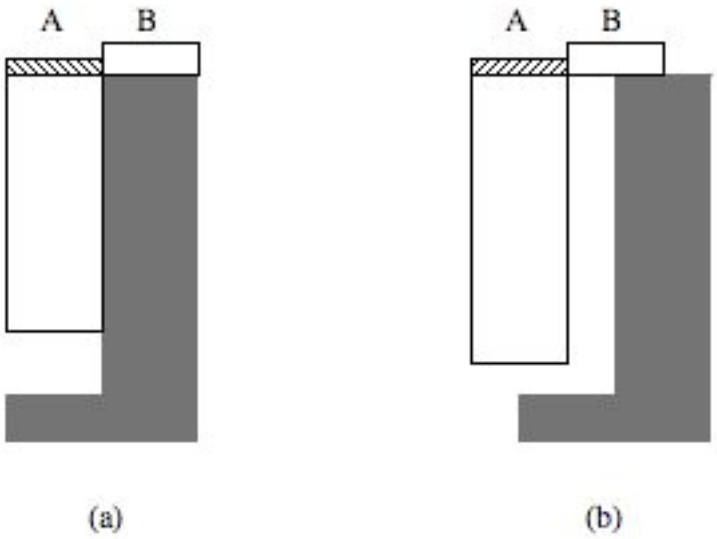

Figure 1: Limiting mass and momentum fluxes near bottom topography. (a) Mass. The dark region indicates bottom topography, and the boxes indicate the mass in a given layer in mass cells A and B. The shaded subregion at the top of cell A illustrates the available mass at the cell edge, for the case where the advective velocity at that edge is positive. If this velocity is negative, then the available mass in the given layer is the entire content of cell B. (b) Momentum. This similar to (a), except that the momentum cells are centered at velocity points, which lie on the edges of mass cells.

of this magnitude is physically reasonable, and in addition it can set up a lateral pressure gradient in layer r which can generate large and irregular velocities.

For such situations, define the "available mass" in layer r at a cell edge to be the amount of mass in the cell in the upstream direction that lies above the stairstep bottom topography. In Figure 1(a) the available mass for the case $u_r > 0$ is illustrated by the shaded subregion at the top of the boxed region in cell A. The upwind method can be modified by defining the mass flux at a cell edge to be the normal velocity at that edge times the density of *available* mass (i.e., available mass per unit horizontal area) in the upstream direction. In the situation illustrated in Figure 1(a), the available masses for the two cases $u_r > 0$ and $u_r < 0$ are similar. Transfers of mass between cells A and B would have similar magnitudes for advective velocities of similar magnitudes but opposite signs.

If the multi-dimensional positive definite advection transport algorithm of Smolarkiewicz and collaborators (e.g., [17]) is used, then the upwind scheme is corrected with some antidiffusive iterations. The formulas for such iterations use values of mass quantities, and in the present situation the values of available mass can be used for those quantities. This strategy was used for the computations described in Section 5.

Using the concept of available mass does not prevent the upward movement of fluid along bottom topography. In some upwelling numerical experiments described in Section 5, wind stress at the free surface causes lateral movement of fluid in the upper layer, and the fluid in the lower layer can then well upward along a slanting bottom. When the fluid in one cell reaches sufficient elevation, then with the present strategy it can spill over into an adjacent cell, and the upwelling continues.

The concept of available mass can be formulated as follows. Consider the u-point $(x_{i-1/2}, y_j)$ between the mass cells with centers at (x_{i-1}, y_j) and (x_i, y_j). Let $(p'_b)_{i-1/2,j}$ denote the value of p'_b at this u-point. In accordance with the idea of stairstep topography used above and in Section 4.5 of [10] (and also by Bleck and Smith [3]), this value is defined by $(p'_b)_{i-1/2,j} = \min((p'_b)_{i,j}, (p'_b)_{i-1,j})$, i.e., it is the minimum of p'_b in the adjacent mass cells. Equivalently, the elevation z of the bottom topography at a u-point is the maximum of the elevations of the bottom topography in the adjacent mass cells. This idea is equivalent to the concept of "shelf horizon depth" used by Holland and Jenkins [12]. Also let $(p'_{r-1})_{i-1,j}$ and $(p'_{r-1})_{i,j}$ denote the values of baroclinic pressure at the top of layer r at the mass points (x_{i-1}, y_j) and (x_i, y_j), respectively. If the advective velocity at the u-point $(x_{i-1/2}, y_j)$ is positive, then the available mass density in the upstream direction is

$$\min\left\{(\Delta p_r)_{i-1,j}, \quad \max\left[(p'_b)_{i-1/2,j} - (p'_{r-1})_{i-1,j}, \ 0\right]\right\}. \tag{13}$$

(Here, a quantity Δp is termed a "mass" density, even though it is really the weight per unit

horizontal area.) If the advective velocity is negative, the available mass density is

$$\min\left\{(\Delta p_r)_{i,j},\quad \max\left[(p'_b)_{i-1/2,j} - (p'_{r-1})_{i,j},\ 0\right]\right\}. \tag{14}$$

The quantity $\max\left[(p'_b)_{i-1/2,j} - (p'_{r-1})_{i-1,j},\ 0\right]$ in (13) measures the vertical distance, in pressure units, from the bottom topography to the top of layer r in the upstream direction for that case. This quantity is zero if the bottom topography is the higher of the two. Baroclinic pressures are used to determine the vertical distance, as total pressures can include variations in the free-surface elevation and give misleading results. If the vertical distance is greater than the thickness $(\Delta p_r)_{i-1,j}$, then the entire layer r in the upstream cell is available, as indicated by (13); otherwise, only the portion above the bottom topography is available. The increment Δp_r in total pressure is used here instead of the baroclinic pressure increment $\Delta p'_r$, in anticipation of solving the mass conservation equation for total pressure as described in Section 3.4.

The concept of available mass is consistent with the process of solving the barotropic mass equation (6), in the case where the values of p'_b at velocity points are defined as above. In that equation, the mass fluxes in the x- and y-directions are $p'_b\bar{u}$ and $p'_b\bar{v}$, respectively. In a straightforward discretization of (6) the mass flux at u-point $(x_{i-1/2}, y_j)$ can be taken to be $(p'_b\bar{u})_{i-1/2,j}$, i.e., it is the value of $\bar{u}$ at that point times the depth of fluid (in pressure units) lying above the stairstep bottom topography. When modeling the transport of mass within an individual layer, it is then consistent to consider only the portion of the layer that lies above the bottom topography. This point will turn out to be significant for a flux adjustment process described in Section 3.4.

Figure 1(b) is similar to Figure 1(a) and illustrates the situation for momentum flux. With the C-grid, momentum cells are centered at the edges of mass cells, and this accounts for the difference between the two pictures. In analogy with the preceding discussion, define the "available momentum" at the edge of a u-momentum cell to be the proportion of the upstream cell that lies above elevation of the bottom topography at the u-point, times the momentum density $u'_r\Delta p'_r$ in the upstream cell. If this concept is not used, then a small portion of the momentum in a thick momentum cell can be transferred into a thin momentum cell, and this translates into a large velocity that can violate the Courant-Friedrichs-Lewy condition. For an analogy, consider a cannon ball and a tennis ball traveling at the same velocity; if a small percentage of the momentum in the cannon ball is transferred to the tennis ball, then the latter will begin moving very quickly indeed. The concept of available momentum can be formulated in a manner similar to (13)–(14), and the details will be omitted here.

3.3 Solution of the barotropic equations

The barotropic subsystem (5)–(6) can be solved implicitly with the same Δt that is used for the baroclinic subsystem, or it can be solved explicitly with many short substeps. In the numerical tests of the two-level method described in [10], the barotropic equations were solved with an adaptation of an alternating-direction implicit (ADI) method that was used by Bates [1] for the shallow water equations for a single-layer fluid. However, in the more recent numerical computations involving Rossby waves that are reported in Section 5.1 of the present paper, one of the tests involves a pure external Rossby wave. This test mainly exercises the barotropic solver, and with the ADI method the computed solution is highly inaccurate. With a long baroclinic Δt one would not expect to resolve the rapidly moving external gravity waves, in any case. Given that a slower Rossby wave is also not represented accurately with this ADI method, it seems advisable to consider an alternative for solving the barotropic equations.

One simple option is an explicit forward-backward method that was used by Bleck and Smith [3], in which the mass equation is advanced with a forward step and the results are then used to advance the momentum equations. This method was used successfully in the computations described in Section 5. Denote the barotropic time increment by $\Delta\bar{t} = \Delta t/N$, where Δt is the baroclinic time increment and N is the number of barotropic substeps per baroclinic step. The mass variable $p'_b\eta$ is advanced from barotropic substep m to substep $m+1$ with

$$p'_b\eta^{m+1} \;=\; p'_b\eta^{m} \;-\; (\Delta\bar{t})\nabla\cdot(p'_b\bar{\mathbf{u}})^m. \tag{15}$$

For notational simplicity, discretizations with respect to x and y are not represented here. If m is even, advance the barotropic velocity components $\bar{u}$ and $\bar{v}$ by

$$\begin{aligned} \bar{u}^{m+1} &= \bar{u}^m + (\Delta\bar{t})\left[f\bar{v}^m - \overline{\frac{\partial M}{\partial x}}^{m+1}\right] \\ \bar{v}^{m+1} &= \bar{v}^m + (\Delta\bar{t})\left[-f\bar{u}^{m+1} - \overline{\frac{\partial M}{\partial y}}^{m+1}\right], \end{aligned} \tag{16}$$

and if m is odd use

$$\begin{aligned} \bar{v}^{m+1} &= \bar{v}^m + (\Delta\bar{t})\left[-f\bar{u}^m - \overline{\frac{\partial M}{\partial y}}^{m+1}\right] \\ \bar{u}^{m+1} &= \bar{u}^m + (\Delta\bar{t})\left[f\bar{v}^{m+1} - \overline{\frac{\partial M}{\partial x}}^{m+1}\right]. \end{aligned} \tag{17}$$

Once an updated value of a velocity component is computed, it is used immediately in the Coriolis term for the other component. The alternation of order between even and odd steps

provides an unbiased treatment of the Coriolis terms, and it resembles the operator splitting of Strang [18]. The quantities $\overline{\partial M/\partial x}$ and $\overline{\partial M/\partial y}$ are mass-weighted vertical averages, as formulated by Higdon [9]. The algorithm as described by Bleck and Smith [3] does not use these averages, but instead it uses the approximations $\alpha_0 \partial(p'_b\eta)/\partial x$ and $\alpha_0 \partial(p'_b\eta)/\partial y$, where α_0 is a representative value of specific volume.

Following are some remarks that are not restricted to the time-stepping method (15)–(17), but instead apply more generally. The quantities $\overline{\partial M/\partial x}$ and $\overline{\partial M/\partial y}$ involve the barotropic mass variable $p'_b\eta$, with coefficients that involve baroclinic quantities. In the particular case of (16)–(17), the values of $p'_b\eta$ are taken from time level $m+1$, as indicated by the superscripts on $\overline{\partial M/\partial x}$ and $\overline{\partial M/\partial y}$. During the prediction step from baroclinic time t_n to baroclinic time t_{n+1}, the baroclinic coefficients are equal to their values at time t_n, and during the correction step these are averages of values from times t_n and t_{n+1}.

An alternative to holding these coefficients constant during the correction step would be to interpolate linearly in t. Higdon and de Szoeke [11] used such an interpolation during linearized stability analyses of two different time-stepping schemes for the coupled barotropic-baroclinic system, and in each case the amplitudes of the eigenvalues of the amplification matrix show extremely narrow spikes as a function of wavenumber. In these analyses the barotropic equations were solved exactly in t in order to isolate the effects of the barotropic-baroclinic splitting and the overall time-stepping scheme. Subsequent analyses (unpublished) indicated that the spikes disappear when the baroclinic coefficients are averaged and not interpolated. Accordingly, interpolation was not considered during the later linearized stability analysis of the two-level method given in [10].

One consequence of using constant values for the baroclinic coefficients of $p'_b\eta$ in $\overline{\partial M/\partial x}$ and $\overline{\partial M/\partial y}$ is that the barotropic subsystem experiences a small discontinuity in t in the pressure forcing between consecutive baroclinic time intervals. In some tests involving external Rossby waves, noise eventually developed in the barotropic subsystem, and this was apparently due to the repeated impulsive forcing caused by the discontinuity. This noise was successfully removed by the following process.

Let $\bar{u}^0$, $\bar{v}^0$, and $p'_b\eta^0$ denote the values of the barotropic variables at the beginning of a (long) baroclinic time interval. Compute the solution at the first barotropic step, and then compute the averages $\bar{u}^{1/2} = (\bar{u}^0 + \bar{u}^1)/2$, $\bar{v}^{1/2} = (\bar{v}^0 + \bar{v}^1)/2$, and $p'_b\eta^{1/2} = (p'_b\eta^0 + p'_b\eta^1)/2$. This averaging is done in order to filter sawtooth behavior in t, but for smooth solutions this process is second-order accurate in t. If the barotropic computation is then carried forward with the values $\bar{u}^{1/2}$, $\bar{v}^{1/2}$, and $p'_b\eta^{1/2}$ and with time increment $\Delta\bar{t}$, the computation will yield the solution at half-integer barotropic steps and thus will not end exactly at the end of the baroclinic time interval. Accordingly, compute for one step to produce $\bar{u}^{3/2}$, $\bar{v}^{3/2}$, and $p'_b\eta^{3/2}$.

Repeat the averaging process to obtain $\bar{u}^1$, $\bar{v}^1$, and $p'_b\eta^1$, and then continue on to the end of the baroclinic time interval without any further averaging. This process was used in the numerical computations reported in Section 5.

The computational cost of solving the barotropic equations explicitly with short substeps, relative to the cost of the remainder of the algorithm, depends on the number of layers and on the number of barotropic substeps per baroclinic step. The latter depends on the ratio of the external wave speed to the largest of the internal wave speeds, which in turn depends on the thicknesses and densities of the various layers. In the tests involving Rossby waves in a two-layer fluid reported in Section 5.1, there are 35 barotropic substeps per baroclinic step. In that case the computational time spent on the barotropic subsystem, for the prediction and correction steps combined, was a little less than half the total computational time. In other words, the computational cost of the barotropic subsystem was comparable to that of two layers. Here, a serial workstation was used. As the number of layers increases, the time spent on the barotropic equations remains constant, whereas the cost of the remainder of the algorithm increases proportionately.

3.4 Conservation of mass

With the barotropic-baroclinic splitting outlined in Section 2.2, the mass equation (7) can be used to update the baroclinic layer thickness $\Delta p'_r$. However, this equation is not in conservation form, and numerical experiments have shown that this equation does not yield conservation of mass in each layer. The purpose of the present subsection is to outline an alternate method that yields exact conservation of mass in each layer, up to roundoff error.

The main idea of this method is to use the mass equation (2) in the unsplit system and enforce a kind of consistency between (2) and the barotropic mass equation (6). Various versions of this strategy have also been used by other investigators, as described below. The purpose of the present subsection is to give one formulation and exposition of this approach and to contribute to a complete description of the methods that are used in the numerical computations described in Section 5.

A reason for seeking exact conservation is the following. In the governing equations (1)–(3) considered in the present paper, it is assumed for simplicity that there is no transfer of mass between layers. However, a realistic isopycnic model would allow for such transfers. Vertical diffusion of heat and/or salt can cause movement of surfaces of constant density (e.g., de Szoeke and Springer [4]), so an observer located on such a surface would witness fluid parcels crossing that surface. If density (or a related quantity) is used as the vertical coordinate, then the vertical diffusion of heat and/or salt is manifested by a transport of mass between layers. Now suppose that a numerical algorithm allows spurious transports

of mass between layers in situations where the governing equations do not admit physical transports. If such an algorithm is then applied to situations where physical transports can take place, the computed results will contain a combination of physical transports and spurious numerical effects. This process can compromise the accuracy of simulations in which thermodynamic effects are important, such as long-term climate simulations.

The mass equation (2) in the unsplit system is in conservation form, and exact conservation of mass in each layer (up to roundoff error) would be obtained by using this equation instead of the baroclinic equation (7). However, the quantity Δp_r in (2) is the total layer thickness, and it fully contains the effects of rapidly-moving external gravity waves. If this equation is solved with a value of Δt that is appropriate for resolving the slow motions in the system, then there is a danger of computational instability. This prospect is the reason for (approximately) splitting the fast and slow motions into separate subproblems.

In order to investigate this issue, first consider a two-layer fluid for which the flow is a small perturbation of a stationary state having a level free surface, a level interface between layers, and a level bottom. This is the same situation considered in the linearized stability analysis in [10]. Let $\Delta\tilde{p}_r$ denote the equilibrium thickness of layer r (in pressure units) for $r = 1, 2$. Also let Δp_r and $\Delta p'_r$ denote the perturbations in total thickness and baroclinic thickness, respectively, of layer r. In this notation, the pressure splitting defined in Section 2.2 is $\Delta\tilde{p}_r + \Delta p_r = (1 + \eta)(\Delta\tilde{p}_r + \Delta p'_r)$; if the product of the small quantities η and $\Delta p'_r$ is neglected, the result is the linearized splitting $\Delta p_r = \Delta p'_r + \eta\Delta\tilde{p}_r$. In this same notation, the layer thickness equation (2) can be written in the linearized form

$$\frac{\partial}{\partial t}\left(\Delta p_r\right) + \Delta\tilde{p}_r \nabla \cdot \mathbf{u}_r \;=\; 0. \tag{18}$$

When the linearized pressure splitting is inserted into (18), along with the relation $\mathbf{u}_r = \bar{\mathbf{u}} + \mathbf{u}'_r$, the result is

$$\frac{\partial}{\partial t}\left(\Delta p'_r\right) + \Delta\tilde{p}_r \nabla \cdot \mathbf{u}'_r + \Delta\tilde{p}_r \left[\frac{\partial \eta}{\partial t} + \nabla \cdot \bar{\mathbf{u}}\right] \;=\; 0. \tag{19}$$

The quantities $\Delta p'_r$ and η approximately represent the separation of the mass field into slowly-varying and rapidly-varying quantities, respectively, so equation (19) displays explicitly the multiple time scales contained in (18).

However, equation (18) would not be used in isolation, but instead would be used here as part of a coupled barotropic-baroclinic splitting. In the present linearized setting, the barotropic mass equation (6) is

$$\frac{\partial \eta}{\partial t} + \nabla \cdot \bar{\mathbf{u}} \;=\; 0; \tag{20}$$

when (20) is inserted into (19), the result is

$$\frac{\partial}{\partial t}\left(\Delta p_r'\right) + \Delta\tilde{p}_r \nabla \cdot \mathbf{u}_r' \;=\; 0, \tag{21}$$

which is the linearization of the baroclinic mass equation (7). Using the total mass equation (18)–(19) in conjunction with the barotropic mass equation (20) is thus equivalent to using the baroclinic mass equation (21) with the barotropic equation (20).

The latter pairing, of (20) and (21), was used in the linearized stability analysis of the two-level method in [10], and the conclusion of that analysis was that the algorithm is stable in the linear case. The preceding discussion suggests that if the equation (2) for total thickness Δp_r (not the baroclinic thickness $\Delta p_r'$) is used in the barotropic-baroclinic splitting, and if the results from the barotropic mass equation (6) are incorporated into the implementation of (2) in some appropriate manner, then it might be possible to obtain an algorithm that behaves stably. The question is how to do this.

The approach used here is to adjust the lateral mass fluxes in individual layers so that the vertical sum of these fluxes equals the flux used for the barotropic mass equation (6), at each edge of each mass cell. These adjustments maintain conservation form, so the total mass in each layer is conserved. The idea of flux adjustment is implicit in a method of Hallberg [8]; during a discussion of a split-explicit time-stepping method, Hallberg mentions briefly that he modifies the mass equation in each layer so that the barotropic velocity equals the mass-weighted vertical average of the advective velocities that are used to advance the layer thicknesses. Multiplication by bottom pressure yields a statement about mass fluxes. Hallberg states that this modification to the layer thickness equation filters the fast external gravity waves from that equation. Related ideas involving flux adjustment have recently been developed by Mats Bentsen (personal communication) and John Dukowicz (personal communication and [5]), and their formulations and experiences will be reported elsewhere.

In the version described below, the flux adjustment is done in an upwind manner in order to preserve nonnegative layer thicknesses, and the concept of available mass described in Section 3.2 is used for the sake of implementation with variable bottom topography. Numerous numerical experiments with zero explicit viscosity over long time intervals suggest numerical stability of this scheme. In addition, these experiments indicate that the mass in each layer is conserved exactly, up to roundoff error.

With the two-level time-stepping method described in [10], the layer thickness is updated after the barotropic variables are predicted. When the barotropic equations are mentioned in the following discussion, the results from the prediction step can be assumed. Once the updated values of layer thicknesses are computed and adjusted, they are used immediately to compute forcing terms at the new time t_{n+1}. With the two-level scheme the barotropic

variables are later corrected, and afterward the flux adjustment mentioned in equation (29) is applied again, so as to ensure consistency between the final values of layer mass variables and the barotropic mass variable.

Suppose that equation (2), $\partial(\Delta p_r)/\partial t + \nabla\cdot(\mathbf{u}_r \Delta p_r) = 0$, is approximated in a given mass cell with a conservative scheme of the form

$$\Delta p_r^{n+1} \;=\; \Delta p_r^n + \frac{\Delta t}{\Delta x}\left[F_r^{x-} - F_r^{x+}\right] + \frac{\Delta t}{\Delta y}\left[F_r^{y-} - F_r^{y+}\right]. \tag{22}$$

Here, F_r^{x-} is a value of mass flux (with units of velocity times pressure) at the edge of the cell corresponding to minimal x, F_r^{x+} is a flux at the edge corresponding to maximal x, and F_r^{y-} and F_r^{y+} are analogous quantities in the y-direction. Now sum (22) over all layers ($1 \le r \le R$), and observe that the sum of Δp_r over all layers is equal to the bottom pressure $p_b = p_b' + p_b'\eta$, to obtain

$$p_b'\eta^{n+1} \;=\; p_b'\eta^n \;+\; \frac{\Delta t}{\Delta x}\left[\sum_{r=1}^{R} F_r^{x-} - \sum_{r=1}^{R} F_r^{x+}\right] \;+\; \frac{\Delta t}{\Delta y}\left[\sum_{r=1}^{R} F_r^{y-} - \sum_{r=1}^{R} F_r^{y+}\right]. \tag{23}$$

The bottom pressure perturbation $p_b'\eta^{n+1}$ can also be computed by using the barotropic mass equation (6), $\partial(p_b'\eta)/\partial t + \nabla\cdot(p_b'\bar{\mathbf{u}}) = 0$. Suppose that this equation is solved explicitly with time increment $\Delta\bar{t} = \Delta t/N$, where N is the number of barotropic substeps of the baroclinic time interval $[t_n, t_{n+1}]$. The algorithm at each substep can be written in the form

$$p_b'\eta^{n,m+1} \;=\; p_b'\eta^{n,m} \;+\; \frac{\Delta\bar{t}}{\Delta x}\left[(H^{x-})^m - (H^{x+})^m\right] \;+\; \frac{\Delta\bar{t}}{\Delta y}\left[(H^{y-})^m - (H^{y+})^m\right], \tag{24}$$

where $p_b'\eta^{n,0} = p_b'\eta^n$; $p_b'\eta^{n,N} = p_b'\eta^{n+1}$; and $(H^{x\pm})^m$ and $(H^{y\pm})^m$ are values of $p_b'\bar{u}$ and $p_b'\bar{v}$, respectively, at the appropriate cell edges. Summation of (24) over all barotropic substeps yields

$$\begin{aligned} p_b'\eta^{n+1} \;=\; p_b'\eta^n \;&+\; \frac{\Delta t}{\Delta x}\left[\frac{1}{N}\sum_{m=0}^{N-1}(H^{x-})^m \;-\; \frac{1}{N}\sum_{m=0}^{N-1}(H^{x+})^m\right] \\ &+\; \frac{\Delta t}{\Delta y}\left[\frac{1}{N}\sum_{m=0}^{N-1}(H^{y-})^m \;-\; \frac{1}{N}\sum_{m=0}^{N-1}(H^{y+})^m\right], \end{aligned} \tag{25}$$

since $\Delta\bar{t} = \Delta t/N$.

Equations (23) and (25) provide two independent methods for computing the perturbation $p_b'\eta$ in bottom pressure (or equivalently, the bottom pressure p_b). These two methods give consistent results if $\sum_{r=1}^{R} F_r = \frac{1}{N}\sum_{m=0}^{N-1}(H)^m$ at each cell edge, i.e., if the vertical sum of the layer fluxes equals the time average of the barotropic flux at each edge. However, in general this is not exactly the case, due to different numerical methods being used in the barotropic and baroclinic subsystems.

One method for enforcing consistency is the following. At a given cell edge e (where $e = x-$, $x+$, $y-$, or $y+$) define the flux deficit

$$D^e \;=\; \frac{1}{N}\sum_{m=0}^{N-1}(H^e)^m \;-\; \sum_{r=1}^{R} F_r^e \tag{26}$$

and then apportion this deficit over all of the layers, in some manner. Here, the deficit is distributed proportionately in a mass-weighted, upwind fashion. Define $\Delta p_r^{e,upwind}$ to be the *available* mass density in layer r at edge e in the upwind direction, where "upwind" is defined by the sign of D^e, "available mass" is defined in Section 3.2, and values of Δp_r are taken from the output from the conservative scheme (22). If $D^e > 0$ the upwind direction is on the negative side of edge e, and if $D^e < 0$ the upwind direction is on the positive side of edge e. Then let $p_b^{e,upwind} = \sum_{r=1}^{R} \Delta p_r^{e,upwind}$; according to the definition of available mass, $p_b^{e,upwind}$ is approximately equal to p_b' at edge e. Now define the flux adjustments

$$A_r^e \;=\; \left(\frac{\Delta p_r^{e,upwind}}{p_b^{e,upwind}}\right) D^e \tag{27}$$

and use these adjustments to modify the scheme (22). More explicitly, the initial application of (22) yields

$$\Delta p_r^* \;=\; \Delta p_r^n + \frac{\Delta t}{\Delta x}\left[F_r^{x-} - F_r^{x+}\right] + \frac{\Delta t}{\Delta y}\left[F_r^{y-} - F_r^{y+}\right]; \tag{28}$$

values of Δp_r^* are used to define the quantities $\Delta p_r^{e,upwind}$ and thus the adjustments A_r^e; and the adjustments are then applied to give

$$\Delta p_r^{n+1} \;=\; \Delta p_r^* + \frac{\Delta t}{\Delta x}\left[A_r^{x-} - A_r^{x+}\right] + \frac{\Delta t}{\Delta y}\left[A_r^{y-} - A_r^{y+}\right]. \tag{29}$$

Combining (28) and (29) yields

$$\begin{aligned}\Delta p_r^{n+1} \;=\; \Delta p_r^n \;&+\; \frac{\Delta t}{\Delta x}\left[(F_r^{x-} + A_r^{x-}) - (F_r^{x+} + A_r^{x+})\right] \\ &+\; \frac{\Delta t}{\Delta y}\left[(F_r^{y-} + A_r^{y-}) - (F_r^{y+} + A_r^{y+})\right].\end{aligned} \tag{30}$$

Now sum (30) over all layers. At each edge e, the vertical sum of the adjusted fluxes is

$$\sum_{r=1}^{R}(F_r^e + A_r^e) \;=\; \sum_{r=1}^{R} F_r^e + D^e\left(\sum_{r=1}^{R}\frac{\Delta p_r^{e,upwind}}{p_b^{e,upwind}}\right) \;=\; \frac{1}{N}\sum_{m=0}^{N-1}(H^e)^m. \tag{31}$$

With the scheme (30), the vertical sum of the lateral mass fluxes over all layers has thus been adjusted to be equal to the time average of the barotropic flux. The layer equations and the barotropic mass equation then give consistent values of bottom pressure, as desired.

In the preceding discussion, the concept of available mass is used to apportion the flux deficit among the various layers, for the following reason. It is possible for a layer r to abut steep bottom topography, at some u-point, and for its upper boundary to lie below the stairstep representation of the topography at that u-point. In that case, the flux in layer r across that u-point should be zero, even after the flux deficit is distributed across various layers. If the available mass is used to determine this distribution, then the zero-flux condition is satisfied, but if total layer thickness Δp_r is used then the zero-flux condition could be violated.

Finally, we point out that nonnegative layer thicknesses are preserved by the process of flux adjustment described above. The flux deficit (26) has units of pressure times velocity. Assume that this deficit is small, in the sense $|D^e| \ll (p'_b)^e U$, where $(p'_b)^e$ is the value of p'_b at edge e, and U is an upper bound on the values of $|u_r|$ and $|v_r|$. Assume that U satisfies a Courant-Friedrichs-Lewy condition of the form $U\Delta t/\Delta x \leq \gamma$ and $U\Delta t/\Delta y \leq \gamma$ for some constant γ that is on the order of 1. In the following, the quantity $\Delta p_r \Delta x \Delta y$ will be referred to as the "mass" in a given grid cell, for convenience, even though Δp_r is actually the weight per unit horizontal area in layer r. For simplicity, also assume uniform grid spacings in x and y.

In the adjustment step (29), consider the contribution to the total mass in a cell due to the flux adjustment at the edge corresponding to minimal x. The effects of the other edges can be described similarly. The magnitude of the change in the total mass $\Delta p_r \Delta x \Delta y$ in the cell due to this edge, over one time step, is

$$\begin{aligned} |\Delta t \Delta y A_r^{x-}| &= \Delta t \Delta y \left(\frac{\Delta p_r^{e,upwind}}{p_b^{e,upwind}} \right) |D^e| \\ &\approx \Delta t \Delta y \Delta p_r^{e,upwind} \frac{|D^e|}{(p'_b)^e} \ll \Delta t \Delta y \Delta p_r^{e,upwind} U. \end{aligned}$$

(Here, $\Delta p_r^{e,upwind} > 0$ is assumed.) This change represents a loss of mass in the cell in the upwind direction. The available mass in that cell, prior to the adjustment step, is $\Delta p_r^{e,upwind} \Delta x \Delta y$. The preceding relations can be re-written in the form

$$|\Delta t \Delta y A_r^{x-}| \ll \frac{U\Delta t}{\Delta x} \Big(\Delta p_r^{e,upwind} \Delta x \Delta y \Big) \leq \gamma \Big(\Delta p_r^{e,upwind} \Delta x \Delta y \Big),$$

where $\gamma \approx 1$. The amount of mass that is transported from the upwind cell, in one adjustment step, is thus far less than the available mass that resides in that cell prior to the adjustment step, provided $\Delta p_r^{e,upwind} > 0$. If $\Delta p_r^{e,upwind} = 0$, then no mass is transported across this edge. It then follows that if a mass cell has nonnegative thickness prior to the adjustment step, then it also has nonnegative thickness after that step.

4 Rossby waves in a two-layer fluid

The goal of the present section is to develop a test problem, involving Rossby waves, which can be used to check the accuracy of time-stepping methods. Rossby waves are slowly-moving waves for which the underlying restoring mechanism is based on vorticity instead of gravity (Pedlosky [13]), and their motion is fundamental to the development of large-scale circulation systems (Gill [7]). The existence of Rossby waves depends on the variation of the Coriolis parameter with respect to latitude and/or variations in bottom topography. Here we assume variations with respect to latitude, and we consider a two-layer fluid in order to test time-stepping methods as applied to the barotropic-baroclinic splitting for multi-layer models. The following analysis yields semi-analytical solutions for which the time evolution is known essentially exactly. Each of these solutions is either a pure internal mode or a pure external mode, and the separation into modes makes it possible to test the baroclinic and barotropic subsystems independently.

In Section 2.3 of [10] the two-level method was applied to a much simpler test problem involving the linearized shallow water equations for a single-layer fluid. In that problem the Coriolis parameter was assumed constant, and Fourier transforms in space yielded a system of ordinary differential equations that could be used to test various time-stepping methods. Compared to the leapfrog method with Asselin filter and two other two-level methods, the present two-level method yielded less phase error and no amplitude error. Because of the assumption of a constant Coriolis parameter, that test problem was limited to gravity waves.

For the present analysis, assume that the flow is a small perturbation of a static state having a level free surface, a level interface between layers, and a level bottom. Let $\Delta\tilde{p}_r$ denote the equilibrium thickness of layer r for $r = 1, 2$; Δp_r denote the perturbation in thickness of layer r; and M_r denote the perturbation in Montgomery potential. The governing equations (1)–(3) can then be written in the linearized form

$$\begin{aligned} \frac{\partial u_r}{\partial t} - f v_r &= -\frac{\partial M_r}{\partial x} \\ \frac{\partial v_r}{\partial t} + f u_r &= -\frac{\partial M_r}{\partial y} \\ \frac{\partial}{\partial t}\left(\Delta p_r\right) + \Delta\tilde{p}_r \left(\frac{\partial u_r}{\partial x} + \frac{\partial v_r}{\partial y}\right) &= 0 \end{aligned} \tag{32}$$

for $r = 1, 2$, with the jump condition

$$M_1 - M_2 = p_1(\alpha_1 - \alpha_2). \tag{33}$$

Here, p_1 denotes the perturbation in pressure at the bottom of layer 1. For purposes of the present analysis, assume that the spatial domain is defined by $-\infty < x < \infty$ and $0 < y < L$,

with solid walls located at the boundaries $y = 0$ and $y = L$. Also assume that the Coriolis parameter f is represented by the linear beta-plane approximation $f(y) = f_0 + \beta(y - \frac{L}{2})$, where β is a positive constant. Here, x and y are regarded as eastward and northward coordinates, respectively.

In situations where f varies with y, it is not possible to develop a test problem that involves a Fourier transform with respect to y. Instead, we discretize the present problem with respect to x and y, leaving t continuous, and then apply Fourier transforms with respect to x and t. The resulting system involves a finite amount of information in the y-direction, and this yields a tractable problem for constructing solutions. For fixed wavenumber in x, this problem is a matrix eigenvalue problem that can be solved numerically. Up to the numerical accuracy in computing eigenvalues and eigenvectors, the analysis yields exact evolution in t for special modal solutions. These can be compared to solutions that are obtained with the same spatial discretization but with numerical time-stepping methods.

Analytical descriptions of Rossby waves in, e.g., [7], [13], [14], entail various approximations in the formulas for frequencies and spatial dependences of these waves. If such results are compared with the results obtained from a numerical model, then the discrepancies between the two results could be due to errors in both the analytical and numerical solutions. The purpose of the present analysis is to produce comparisons in which, for practical purposes, the only errors are due to numerical time-stepping schemes.

Before proceeding further, it is useful to eliminate M_r from the system (32), so that the only unknowns for layer r are u_r, v_r, and Δp_r. Let $\tilde{M}_r$ denote the Montgomery potential in layer r at the equilibrium state; let $\tilde{p}_r$ and $\tilde{z}_r$ denote the pressure and elevation, respectively, at the bottom of layer r at the equilibrium state; and let p_r and z_r denote perturbations in those quantities. The Montgomery potential in layer r is then $\tilde{M}_r = \alpha_r \tilde{p}_r + g\tilde{z}_r$ at the equilibrium state and $\tilde{M}_r + M_r = \alpha_r(\tilde{p}_r + p_r) + g(\tilde{z}_r + z_r)$ at a general state. Therefore $M_r = \alpha_r p_r + g z_r$ for $r = 1, 2$. However, the bottom of layer 2 is always located at $z = \tilde{z}_2$, so the perburbation z_2 is always zero. Thus $M_2 = \alpha_2 p_2 = \alpha_2(\Delta p_1 + \Delta p_2)$. The jump condition (33) then implies $M_1 = M_2 + \Delta p_1(\alpha_1 - \alpha_2) = \alpha_1 \Delta p_1 + \alpha_2 \Delta p_2$. Therefore

$$M_r = \alpha_r \Delta p_1 + \alpha_2 \Delta p_2 \tag{34}$$

for $r = 1, 2$. The relation (34) can then be used to eliminate M_r from the system (32). The coupling between the two layers is expressed by the presence of Δp_1 and Δp_2 in both M_1 and M_2.

Now discretize with respect to x and y, with uniform grid spacings Δx and Δy, respectively, and leave t continuous. Denote the grid points in y by $y_0 = 0$, $y_1 = \Delta y$, ..., $y_N = N\Delta y = L$. Approximate the spatial derivatives in the system (32) with centered

second-order derivatives on a C-grid. The mass points then have the form $(x_m, y_{j-1/2})$ for $j = 1, \ldots, N$; the u-points have the form $(x_{m-1/2}, y_{j-1/2})$ for $j = 1, \ldots, N$; and the interior v-points have the form (x_m, y_j) for $j = 1, \ldots, N-1$. The Coriolis terms are discretized in space with the energy-conserving method of Sadourny [15], as described in Section 3.1.

The Fourier transform with respect to x and t is equivalent to considering solutions of the form

$$\begin{aligned} u_r(x, y_{j-1/2}, t) &= \hat{u}^{(r)}_{j-1/2}\, e^{ikx-i\omega t}, \qquad 1 \le j \le N \\ v_r(x, y_j, t) &= \hat{v}^{(r)}_{j}\, e^{ikx-i\omega t}, \qquad 1 \le j \le N-1 \\ \Delta p_r(x, y_{j-1/2}, t) &= \Delta\hat{p}^{(r)}_{j-1/2}\, e^{ikx-i\omega t}, \qquad 1 \le j \le N \end{aligned} \tag{35}$$

with the solid-wall boundary conditions $\hat{v}^{(r)}_0 = \hat{v}^{(r)}_N = 0$. Represent the effect of differences with respect to x by

$$\frac{iK}{\Delta x} = \frac{1}{\Delta x}\left(e^{ik\Delta x/2} - e^{-ik\Delta x/2}\right),$$

so that $K = 2\sin(k\Delta x/2)$, and represent the effect of averaging with respect to x by

$$A = \frac{1}{2}\left(e^{ik\Delta x/2} + e^{-ik\Delta x/2}\right) = \cos(k\Delta x/2).$$

When the forms (35) are inserted into the system (32)–(34), the result is

$$(-i\omega)\hat{u}^{(r)}_{j-1/2} = \frac{1}{2}A\left[f_{j-1}\hat{v}^{(r)}_{j-1} + f_j\hat{v}^{(r)}_j\right] - \frac{iK}{\Delta x}\left[\alpha_r\Delta\hat{p}^{(1)}_{j-1/2} + \alpha_2\Delta\hat{p}^{(2)}_{j-1/2}\right] \tag{36}$$

$$\begin{aligned} (-i\omega)\hat{v}^{(r)}_j &= -\frac{1}{2}Af_j\left[\hat{u}^{(r)}_{j-1/2} + \hat{u}^{(r)}_{j+1/2}\right] \\ &- \frac{\alpha_r}{\Delta y}\left[\Delta\hat{p}^{(1)}_{j+1/2} - \Delta\hat{p}^{(1)}_{j-1/2}\right] - \frac{\alpha_2}{\Delta y}\left[\Delta\hat{p}^{(2)}_{j+1/2} - \Delta\hat{p}^{(2)}_{j-1/2}\right] \end{aligned} \tag{37}$$

$$(-i\omega)\Delta\hat{p}^{(r)}_{j-1/2} = -\Delta\tilde{p}_r\left[\left(\frac{iK}{\Delta x}\right)\hat{u}^{(r)}_{j-1/2} + \frac{1}{\Delta y}\left(\hat{v}^{(r)}_j - \hat{v}^{(r)}_{j-1}\right)\right], \tag{38}$$

where $f_j = f(y_j)$.

Next represent the system (36)–(38) as a matrix eigenvalue problem for fixed k, with eigenvalue $-i\omega$. Let

$$\begin{aligned} U^{(r)} &= \left(\hat{u}^{(r)}_{1/2},\ \hat{u}^{(r)}_{3/2}, \ldots,\ \hat{u}^{(r)}_{N-1/2}\right)^T \\ V^{(r)} &= \left(\hat{v}^{(r)}_{1},\ \hat{v}^{(r)}_{2}, \ldots,\ \hat{v}^{(r)}_{N-1}\right)^T \\ P^{(r)} &= \left(\Delta\hat{p}^{(r)}_{1/2},\ \Delta\hat{p}^{(r)}_{3/2}, \ldots,\ \Delta\hat{p}^{(r)}_{N-1/2}\right)^T. \end{aligned}$$

Equation (36) yields

$$(-i\omega)U^{(r)} = \frac{1}{2}AF_1V^{(r)} - \left(\frac{iK}{\Delta x}\right)\alpha_rP^{(1)} - \left(\frac{iK}{\Delta x}\right)\alpha_2P^{(2)}, \tag{39}$$

where F_1 is the $N \times (N-1)$ matrix defined by

$$F_1 = \begin{pmatrix} f_1 & & & & \\ f_1 & f_2 & & & \\ & f_2 & f_3 & & \\ & & \ddots & \ddots & \\ & & & f_{N-2} & f_{N-1} \\ & & & & f_{N-1} \end{pmatrix}.$$

Equation (37) yields

$$(-i\omega)V^{(r)} = -\frac{1}{2}AF_2U^{(r)} + \left(\frac{\alpha_r}{\Delta y}\right)D_1P^{(1)} + \left(\frac{\alpha_2}{\Delta y}\right)D_1P^{(2)}, \tag{40}$$

where F_2 is the transpose of F_1, and D_1 is the $(N-1) \times N$ matrix defined by

$$D_1 = \begin{pmatrix} 1 & -1 & & & \\ & 1 & -1 & & \\ & & \ddots & \ddots & \\ & & & 1 & -1 \end{pmatrix}.$$

Finally, equation (38) yields

$$(-i\omega)P^{(r)} = -\Delta\tilde{p}_r\left(\frac{iK}{\Delta x}\right)U^{(r)} + \left(\frac{\Delta\tilde{p}_r}{\Delta y}\right)D_2V^{(r)}, \tag{41}$$

where $D_2 = -D_1^T$.

Now let q denote the $(6N-2) \times 1$ column vector whose components consist of the components of $U^{(1)}$, $V^{(1)}$, $P^{(1)}$, $U^{(2)}$, $V^{(2)}$, and $P^{(2)}$, in that order. Equations (39)–(41) imply

$$(-i\omega)q = Gq, \tag{42}$$

where G is the $(6N-2) \times (6N-2)$ matrix given in block form as

$$G = \begin{pmatrix} 0 & \frac{1}{2}AF_1 & -\left(\frac{iK}{\Delta x}\right)\alpha_1 I & 0 & 0 & -\left(\frac{iK}{\Delta x}\right)\alpha_2 I \\ -\frac{1}{2}AF_2 & 0 & \left(\frac{\alpha_1}{\Delta y}\right)D_1 & 0 & 0 & \left(\frac{\alpha_2}{\Delta y}\right)D_1 \\ -\left(\frac{iK}{\Delta x}\right)\Delta\tilde{p}_1 I & \left(\frac{\Delta\tilde{p}_1}{\Delta y}\right)D_2 & 0 & 0 & 0 & 0 \\ 0 & 0 & -\left(\frac{iK}{\Delta x}\right)\alpha_2 I & 0 & \frac{1}{2}AF_1 & -\left(\frac{iK}{\Delta x}\right)\alpha_2 I \\ 0 & 0 & \left(\frac{\alpha_2}{\Delta y}\right)D_1 & -\frac{1}{2}AF_2 & 0 & \left(\frac{\alpha_2}{\Delta y}\right)D_1 \\ 0 & 0 & 0 & -\left(\frac{iK}{\Delta x}\right)\Delta\tilde{p}_2 I & \left(\frac{\Delta\tilde{p}_2}{\Delta y}\right)D_2 & 0 \end{pmatrix}. \tag{43}$$

Here, I denotes the $N \times N$ identity matrix. The matrix G is a function of the wavenumber k in the x-direction.

For fixed k, equations (42)–(43) define an eigenvalue problem for which the eigenvalue $-i\omega$ yields the angular frequency ω in special solutions of the form (35), and various portions of the eigenvector q give dependences with respect to y of u_1, v_1, Δp_1, u_2, v_2, and Δp_2 in those special solutions. For specific values of model parameters, this eigenvalue problem can be solved numerically to yield initial data for testing time-stepping methods.

For example, consider the case where $\Delta x = \Delta y = 10$ km, the width of the channel is 320 km, the Coriolis parameter defines a β-plane centered at 45° N, and the upper and lower layers have equilibrium thicknesses of 1000 meters and 3000 meters and specific volumes of $.975 \times 10^{-3}$ m^3/kg and $.972 \times 10^{-3}$ m^3/kg, respectively. Now let $k\Delta x = \pi/16$ and solve the eigenvalue problem (42)–(43) with these choices of parameters. The resulting distribution of values of ω is indicated in Figure 2. The vertical axis shows values of $|\omega|$ on a logarithmic scale. The horizontal axis indicates the mode number, which is simply a matter of the ordering of the eigenvalue-eigenvector pairs given by the software that is used to compute these quantities.

In this figure, the values of $|\omega|$ lie in three distinct clusters. If the Coriolis parameter is replaced by the constant value associated with latitude 45° N, then the lowermost (right) cluster disappears from the given graph frame, and an inspection of numerical output indicates that the values of $|\omega|$ for this cluster become essentially zero. On the other hand, the values of $|\omega|$ in the other two clusters are essentially unchanged. The modes in the lowermost cluster in Figure 2 are thus Rossby modes, as the existence of such modes depends on the variation of the Coriolis parameter.

The remaining modes are gravity waves. In the case of the uppermost cluster in Figure 2, an inspection of the spatial variations in these modes (not shown here) reveals that the two layers thicken or thin by approximately the same proportion, at each (x, y, t). On the other hand, in the case of the second cluster the perturbations in layer thickness always have opposite signs and nearly cancel, so that the free surface remains nearly level. The modes in the first cluster are thus external waves, and the modes in the second cluster are internal waves. In addition, both the external and internal clusters include Poincaré modes, for which the dependences with respect to y are approximately sinusoidal, and Kelvin modes, which decay exponentially with distance from one or the other of the solid boundaries. This behavior is analogous to descriptions given by Pedlosky ([13], [14]) of channel modes that are solutions of the linearized shallow water equations for a single-layer fluid.

Next consider the structure of the Rossby modes. Figure 3 shows dispersion relations for each of these modes. In this figure, the horizontal axis represents the dimensionless

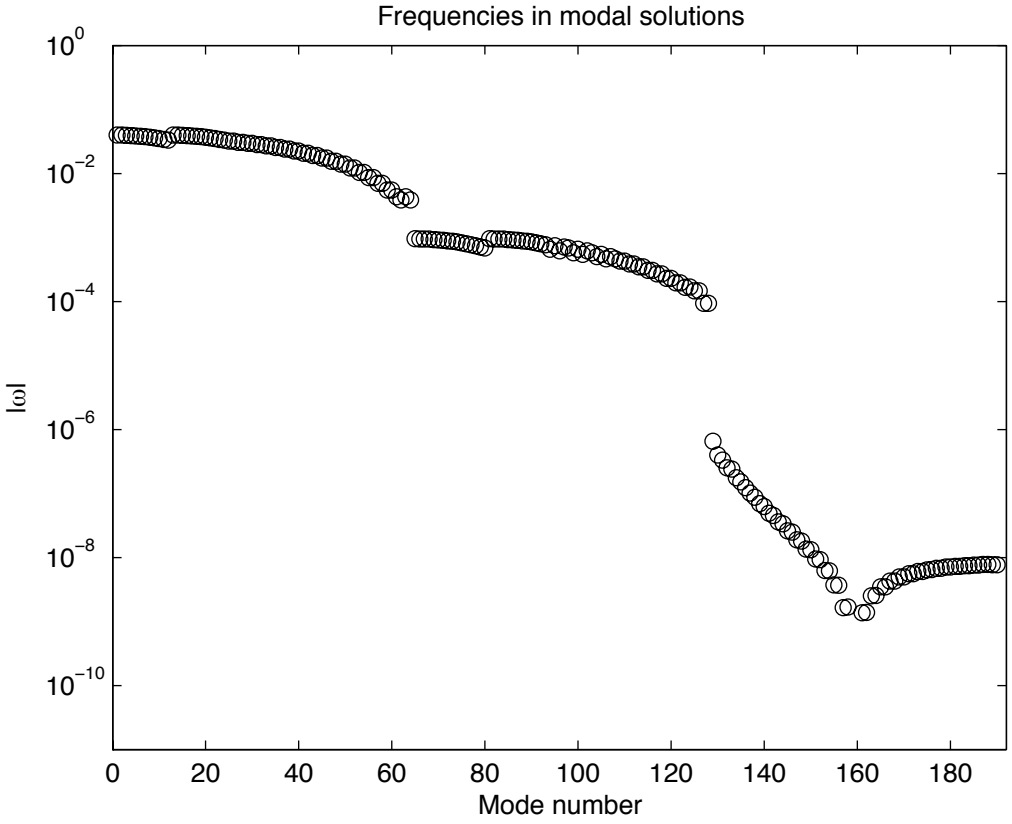

Figure 2: Values of $|\omega|$ for modes in a two-layer fluid in a channel. In this example, $k\Delta x = \pi/16$; $\Delta x = \Delta y = 10$ km; the width of the channel is 320 km; the equilibrium thicknesses of the upper and lower layers are 1000 meters and 3000 meters, respectively; the specific volumes of the upper and lower layers are $.975 \times 10^{-3}$ m^3/kg and $.972 \times 10^{-3}$ m^3/kg, respectively; and the Coriolis term defines a β-plane centered at 45° N. The uppermost (left) cluster of points corresponds to external gravity (Poincaré and Kelvin) modes, the second cluster corresponds to internal gravity modes, and the third cluster corresponds to external and internal Rossby modes.

wavenumber $k\Delta x$ for $0 \leq k\Delta x \leq \pi$, and the vertical axis represents corresponding values of the angular frequency ω. To produce this plot, the eigenvalue problem (42)–(43) was solved for values of $k\Delta x$ varying from 0 to π in increments of $\pi/400$. The values of ω corresponding to the Rossby modes were then sorted and plotted. An inspection of spatial dependences shows that both external and internal Rossby modes are represented here. The dependences with respect to y are nearly sinusoidal, and for a given y-dependence the corresponding external mode has a higher frequency than the corresponding internal mode.

Figure 3 shows the strongly dispersive nature of Rossby waves. The velocity of energy propagation is the group velocity $d\omega/dk$, and for physical Rossby modes this velocity is negative for relatively small values of $|k|$, whereas for relatively large $|k|$ the group velocity is positive. In other words, long Rossby waves propagate energy westward and short Rossby waves propagate energy eastward. The asymmetry of Rossby waves helps to account for the east-west asymmetry in ocean circulation patterns, in which narrow boundary currents are found along western boundaries of ocean basins but not along eastern boundaries (Gill [7]).

The numerical Rossby modes plotted in Figure 3 generally show the same behavior as physical Rossby modes. However, some of the lower-frequency modes show a reversal in the sign of ω, which then implies a reversal in the sign of the group velocity. Plots of the spatial variations in these modes (not shown here) indicate that these modes are highly oscillatory in y, to the point of being nearly grid-scale, so for smooth solutions these modes would be relatively insignificant. In addition, further experiments with varying channel widths suggest that the ratio of maximum $|\omega|$ for these modes to the maximum $|\omega|$ over all modes decreases as the width of the channel increases, so that the anomalous behavior is unlikely to be significant in basin-scale simulations. As noted earlier, in this analysis the Coriolis terms are discretized in (x, y) on a C-grid by using the energy-conserving method of Sadourny [15]. Further experiments (not shown here) indicate that if the Coriolis terms are represented with simple four-point averages, then the reversal of sign does not occur, and $\omega < 0$ for all numerical Rossby modes.

The spatial structures of some Rossby modes are shown in Figures 4–6. Here, the values of physical parameters are the same as those used to obtain Figure 2. The spatial structures of the modes in Figures 4–6 were obtained from the formulas for Δp_1 and Δp_2 that are given in (35), with $t = 0$ and values of $\Delta\hat{p}^{(r)}_{j-1/2}$ taken from the appropriate portions of the corresponding eigenvector of (42)–(43). In each figure the upper graph is a contour plot of the elevation of the free surface at the top of the fluid, and the lower graph is a contour plot of the elevation of the interface between the two layers. In each figure the upper and lower figures use the same contour interval, but no particular scale is used here due to the linearity of the solution. Solid contours indicate positive perturbations in elevation, and

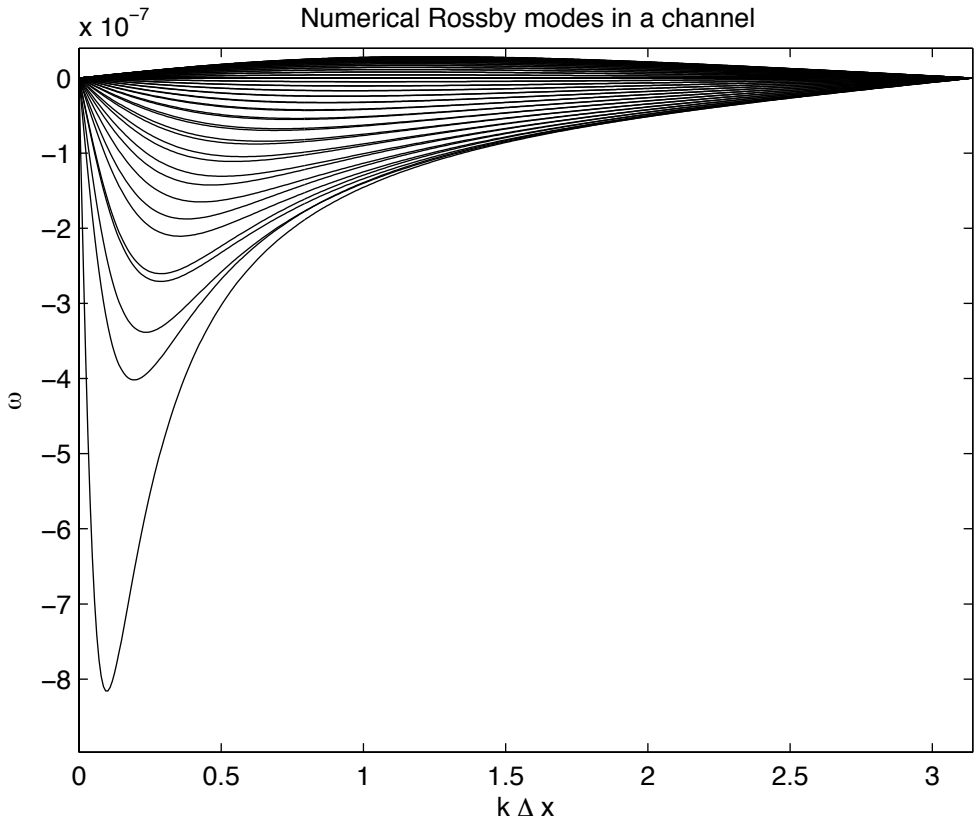

Figure 3: Dispersion relations for Rossby waves in a two-layer fluid in a channel. The horizontal axis represents the dimensionless wavenumber $k\Delta x$, and the vertical axis represents the angular frequency ω. The physical parameters are the same as in Figure 2, except that the values of $k\Delta x$ are sampled from the interval $[0, \pi]$ in increments of $\pi/400$. Each curve represents the dispersion relation for one Rossby mode in the semi-discrete problem obtained by discretizing in space on a C-grid and leaving t continuous. The Sadourny energy-conserving method is used to discretize the Coriolis terms in space. Both external and internal Rossby modes are shown here.

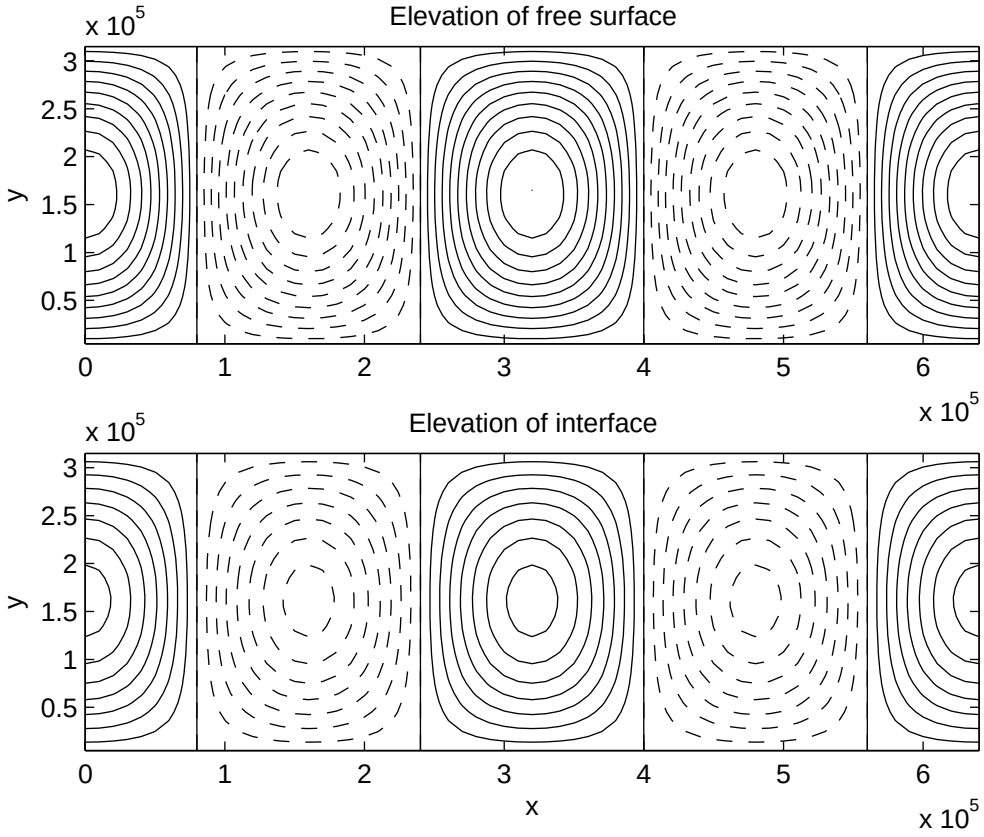

Figure 4: First external Rossby mode for a fixed value of time t. The physical parameters are the same as in Figure 2. The upper graph is a contour plot of the elevation of the free surface at the top of the upper layer, and the lower graph is a contour plot of the elevation of the interface between the two layers. Solid curves indicate positive elevation relative to equilibrium, and dashed curves indicate negative elevation relative to equilibrium. With an external mode, all fluid layers thicken or thin by approximately the same proportion, so in the present case the perturbations in the elevations of the free surface and interface always have the same sign. The velocity field (not shown here) is everywhere tangent to curves of constant elevation, due to the geostrophic balance that is found in Rossby waves.

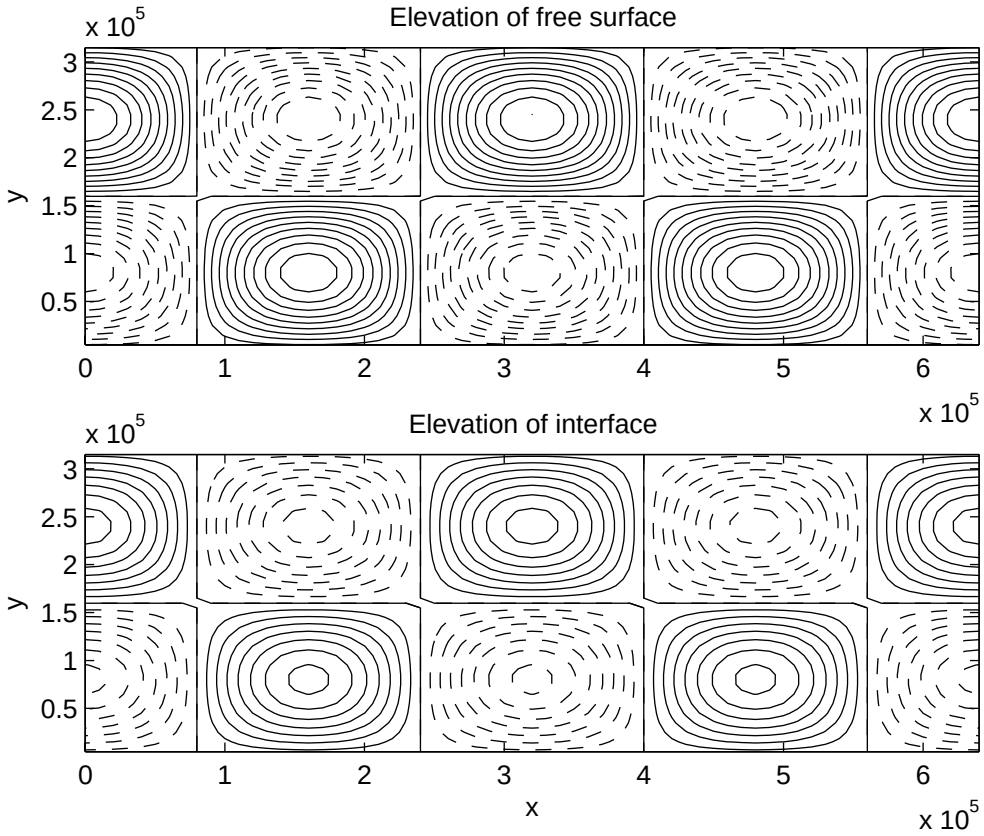

Figure 5: Second external Rossby mode.

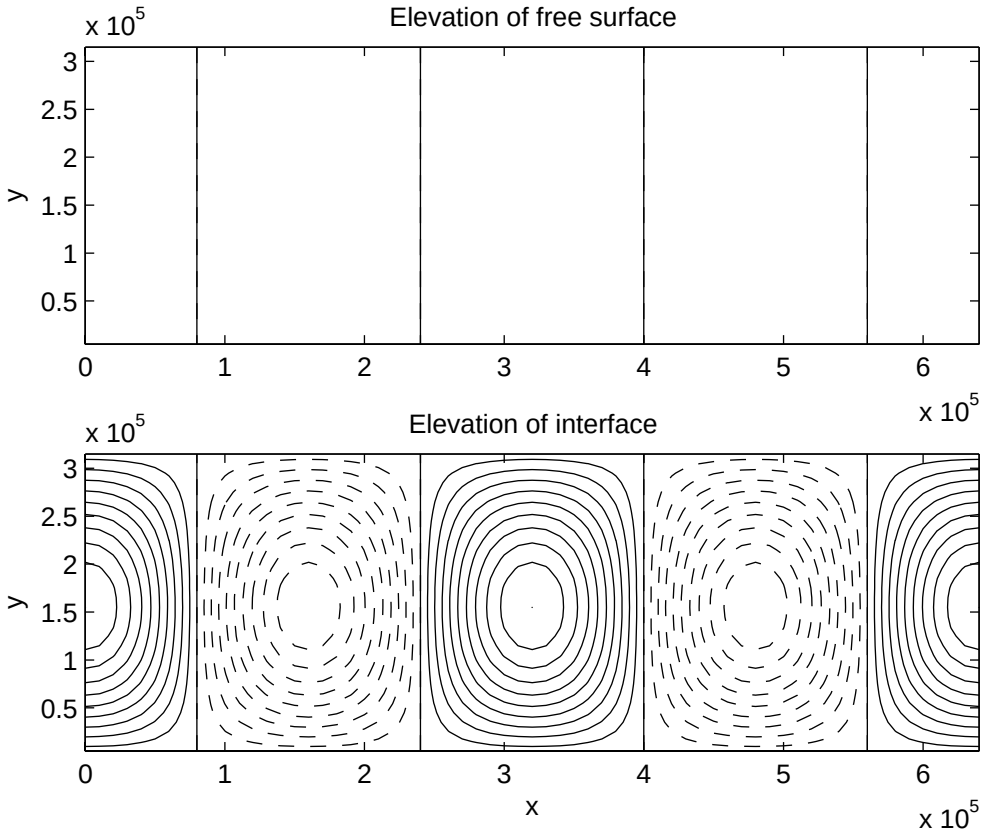

Figure 6: First internal Rossby mode. With an internal mode, the perturbations in the thicknesses of the two layers are of opposite sign and nearly equal magnitude, so the free surface remains nearly level.

dashed contours indicate negative perturbations.

Figure 4 shows the first external Rossby mode. Here, "first" refers to the fact that the dependence with y is the most slowly varying of all the external Rossby modes. The figure illustrates how, at each (x, y, t), the interface and the free surface are either both perturbed upward or both perturbed downward. The movement of the interface is due to variations in the thickness of the lower layer, whereas the movement of the free surface is due to thickening or thinning of both layers, so the perturbations in the free surface are greater than those of the interface. Figure 5 shows the second external Rossby mode, and Figure 6 shows the first internal Rossby mode.

The velocity fields for the Rossby modes are not plotted here, but a summary of their properties is the following. In each of the Rossby modes the velocity field is everywhere tangent to the contours of constant elevation. For such modes the time derivatives (equivalently, frequencies) are sufficiently small that the dominant balance in the momentum equation is between the pressure forcing and the Coriolis term, which is orthogonal to velocity. In the case of external modes the velocity is essentially independent of depth, and in the case of internal modes the velocities in the two layers have opposite directions and have a mass-weighted vertical average that is essentially zero.

For a pure mode, such as those shown in Figures 4–6, the pattern of elevations and velocities translates in the negative direction with phase velocity $\omega/k < 0$. Superpositions of different modes introduce the effects of group velocity that are mentioned above.

For any Rossby mode, as computed from the preceding analysis, the values of layer thicknesses and velocity components for fixed t can be used as initial data for a code that solves the governing equations numerically. Evolution in t that is obtained with the model, at fixed (x, y), can then be compared with the exact evolution that is provided by the above analysis. The results of some comparisons are described in Section 5.1.

5 Numerical computations

This section describes the results of some numerical computations involving the two-level time-stepping scheme and related ideas discussed in this paper. All of the computations involve fluids with two layers. The first set of computations is based on the linear test problem involving Rossby waves that was discussed in Section 4, and it provides a basic test of time-stepping methods. The second set of computations involves variable bottom topography, and in this case the layer thicknesses tend to zero at both the top and bottom of the fluid domain. The third test is a double-gyre experiment in which the flow meanders and forms eddies, and when the explicit horizontal viscosity is set to zero the solution does

not display any numerical grid noise. The lower layer outcrops to the surface in this case as well.

The discussion in this section includes comparisons with a code that uses the leapfrog method for the baroclinic momentum equations but otherwise uses the same ideas as in the code that uses the two-level time-stepping method. In the linear test problem of Section 5.1, the leapfrog version displays substantial effects of the sawtooth computational mode that is allowed by that scheme, whereas the two-level version does not show such effects. In the nonlinear double-gyre experiment of Section 5.3 the leapfrog version crashed, due to an instability that developed near locations where the layer thickness tends to zero.

5.1 Rossby waves

The analysis in Section 4 yields special solutions for which the space and time dependences are known essentially exactly. Values of such solutions at fixed time provide initial data that can then be used in a code that solves the governing equations numerically. In the following, the exact and numerical solutions will be compared as functions of t, at a fixed (x, y) that lies in the middle of the channel. Each of the special solutions is either a pure internal mode or a pure external mode, so these solutions provide a means for testing the barotropic and baroclinic subsystems independently. One effect of the following discussion is to demonstrate a clear choice between two possible methods for solving the barotropic equations.

The physical parameters used here are the same as those used for Figures 2 and 4–6 in Section 4, except that solutions are computed both for $k\Delta x = \pi/16$ and for $k\Delta x = \pi/8$. In the first case there are 32 grid intervals per wavelength in the x (along-channel) direction, and in the second case there are 16 grid intervals per wavelength in the x-direction. Solutions are computed on a spatial domain that extends for 64 mass cells in the x-direction and 32 mass cells in the y (cross-channel) direction. Periodic boundary conditions are used at the boundaries corresponding to maximal and minimal x, in keeping with the periodic nature of the special solutions (35). In these computations the horizontal viscosity A_H in the momentum equation (1) is set to zero. Also, Section 4.4 of [10] describes methods for implementing shear stress between layers and friction at the bottom of the fluid domain, but for the present computations these frictional effects are also set to zero. The time increment used in the baroclinic subsystem is $\Delta t = 1200$ sec, except for the test involving the leapfrog method that is described in Section 5.1.2. The barotropic equations are solved with the explicit method described in Section 3.3, except for one case noted in Section 5.1.3 where these equations are solved implicitly. In the case of the explicit solution, the nominal barotropic time increment is 35 sec; to be more precise, the baroclinic Δt is divided by the nominal barotropic increment, and the result is rounded to the next greatest integer to

obtain the actual number of barotropic subintervals per baroclinic time interval.

The solutions developed in Section 4 are based on a linearization of the governing equations. For the present computations, the solutions are scaled so that the maximum amplitude of fluid velocity (not wave velocity) is one centimeter per second, in order that the dynamics of the fluid are essentially linear. However, the full nonlinear model is used in these computations, not a simplified model specialized for the linear case. In particular, the advective terms in the mass and momentum equations are implemented with the multidimensional positive definite advection transport algorithm (MPDATA), which is described in [17]. This method employs an upwind step followed by antidiffusive corrections, and for the present computations two antidiffusive corrections are used in all cases.

5.1.1 First internal Rossby mode, computed with the two-level method

Figure 7 shows the time dependence for the first internal Rossby mode. (Plots of interface and free-surface elevations for this mode for fixed t are shown in Figure 6 in Section 4.) The upper frame in Figure 7 shows the thickness of the upper layer, in meters, when $k\Delta x = \pi/16$, i.e., when there are 32 grid intervals per wavelength in the x-direction. The solid curve shows the solution obtained from the analysis in Section 4, and the dashed curve shows the solution obtained numerically with the two-level code. There is a very close agreement between these solutions. The lower frame in Figure 7 shows the thickness of the upper layer when $k\Delta x = \pi/8$, i.e., when there are 16 grid intervals per wavelength in the x-direction. In this case some decay can be seen in the solution.

In the analysis of the two-level time-stepping method given in [10], the method was shown to be essentially nondissipative when the barotropic equations are solved exactly in t. In that analysis the Coriolis parameter was assumed constant, unlike the present discussion. If the model parameters for the present computation are applied to the analysis in [10], except for the variation in the Coriolis parameter, and if $k\Delta x = \pi/8$, then the maximum and minimum absolute values of the eigenvalues of the amplification matrix are 1 and approximately $1 - .36 \times 10^{-6}$, respectively. The variation of the solution in t is governed by the powers of these eigenvalues, and for the value of Δt used here the time interval of 1000 days corresponds to 72000 baroclinic time steps. When the eigenvalues are raised to the power 72000, the minimum absolute value is approximately 0.975. If this result for constant Coriolis parameter is relevant to the present computation, then the time-stepping scheme itself does not account for the damping seen in Figure 7. For the present computation the shear stress, bottom stress, and horizontal viscosity are all set to zero. The remaining possible source of damping in the model is the dissipation that is inherent in the advection scheme (MPDATA) that is used for the equations of mass and momentum. The plots in

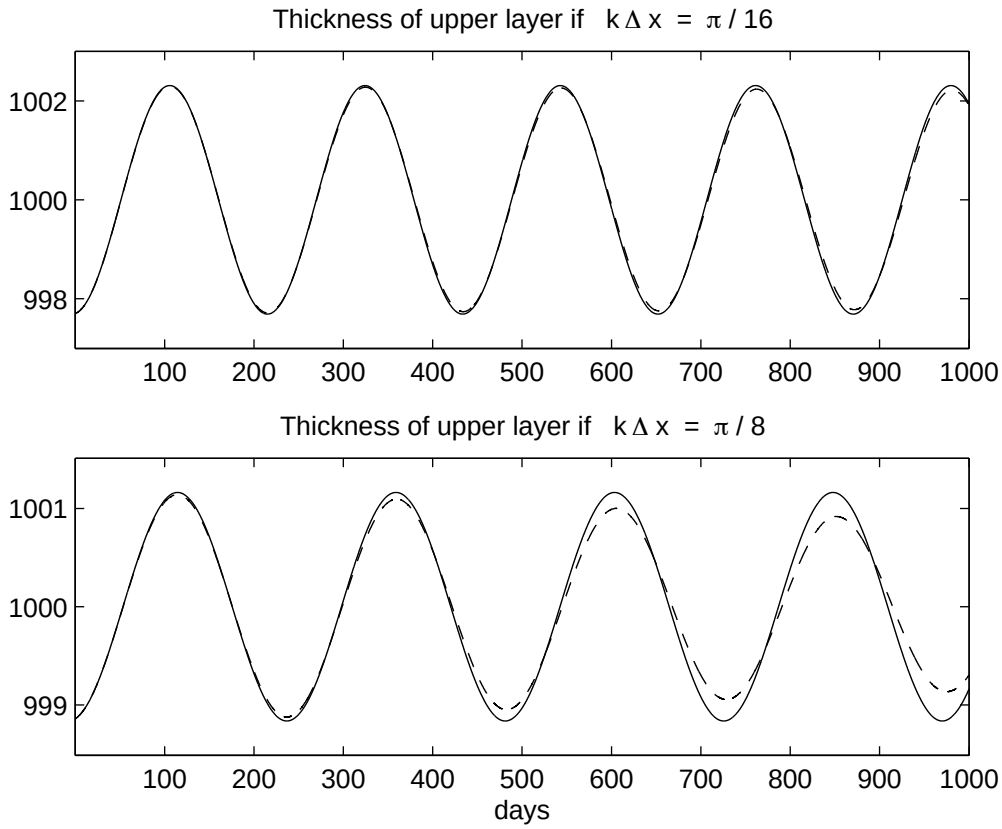

Figure 7: First internal Rossby mode, as computed with a code that employs the two-level time-stepping method described in this paper. Solutions are shown as functions of t at a fixed position in the middle of the channel. The upper frame show the thickness of the upper layer, in meters, when there are 32 grid intervals per wavelength in the x-direction. The lower frame shows the thickness of the upper layer when there are 16 grid intervals per wavelength in the x-direction. In each frame the solid curve is the exact solution obtained from the analysis in Section 4, and the dashed curve is the solution obtained by solving the governing equations numerically. The time-stepping method is essentially nondissipative, so the damping seen in the lower frame is due to the advection scheme (MPDATA) that is used for the equations for mass and momentum. The time interval of 1000 days corresponds to $72,000$ baroclinic time steps, for the value of Δt used here.

Figure 7 then indicate the damping provided by that scheme.

An examination of the computed values of velocities for this example (not shown here) shows that the magnitude of the baroclinic velocity $\mathbf{u}'$ is typically about one to two orders of magnitude larger than the magnitude of the barotropic velocity $\bar{\mathbf{u}}$. The barotropic-baroclinic splitting used here does not provide an exact splitting of the external and internal modes, but the values of velocity do suggest that nearly all of the energy is in the baroclinic system, in the present example. The present computation thus provides a test of the time-stepping used in the baroclinic subsystem, in near isolation from what is done for the barotropic subsystem.

Plots of the thickness of the lower layer (not shown here) indicate patterns that are very similar to those shown in Figure 7. In keeping with properties of internal waves, the perturbation in layer thickness for the lower layer is very nearly the negative of the perturbation for the upper layer, so the sum of the thicknesses of the two layers is nearly constant. This implies that the elevation of the free surface at the top of the fluid is nearly constant, whereas the elevation of the interface between the layers varies more substantially.

5.1.2 First internal mode, computed with the leapfrog method

For the sake of comparison, the preceding problem was also solved with a version of the code that uses the leapfrog method for the baroclinic momentum equations. In this case, the sequence of operations is the following: update baroclinic velocity, predict the barotropic solution, update the layer thicknesses, correct the barotropic solution using time averages of old and new baroclinic mass variables, and compute final values of forcing terms at the new time level. The two-time-level positive definite advection scheme for the layer thicknesses is not replaced with a leapfrog version, in anticipation of using the same code in situations where layer thicknesses could tend to zero. However, for the case of the baroclinic momentum equation, it was not clear how to implement a nonoscillatory advection scheme in the context of the leapfrog method, so instead the nonlinear and Coriolis terms are combined into the form $(\mathbf{u}_r \cdot \nabla)\mathbf{u}_r + f\mathbf{u}_r'^{\perp} = \nabla\left(\frac{1}{2}|\mathbf{u}_r|^2\right) + (\zeta_r + f)\mathbf{u}_r'^{\perp} + \zeta_r\bar{\mathbf{u}}^{\perp}$, where $\zeta_r = \partial v_r/\partial x - \partial u_r/\partial y$. This formula is used, for example, by Bleck and Smith [3]. The result is then discretized with second-order centered differencing and averaging on a C-grid. In particular, the Coriolis/vorticity terms are discretized with the energy-conserving scheme of Sadourny [15].

The leapfrog method requires initial data at two consecutive time levels, so during the first time step the baroclinic momentum equations are solved with a forward step that is implemented with the same subroutine that is used for the prediction step in the two-level version of the code.

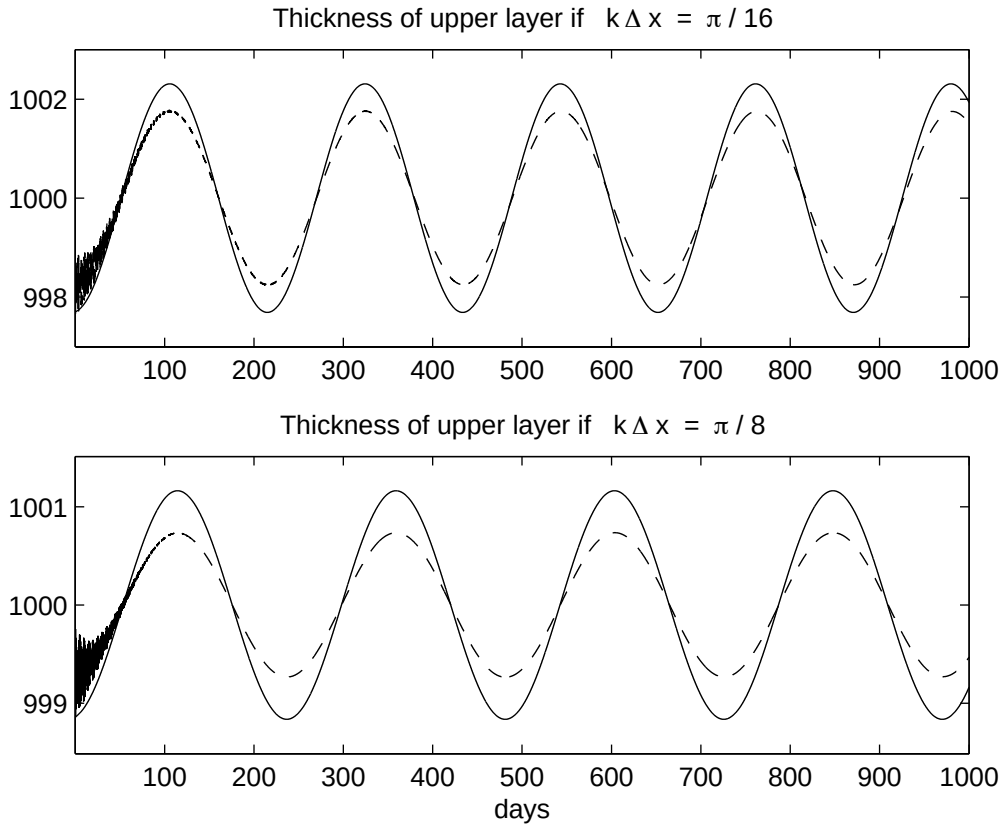

Figure 8: First internal Rossby mode, when the leapfrog method is used for the baroclinic momentum equation. The parameters and format are the same as for Figure 7, except that the baroclinic Δt is cut in half. The noisy behavior at the beginning of the time interval is due to the sawtooth computational mode that is allowed by the leapfrog method, and it is smoothed with an Asselin filter having coefficients $(0.05, 0.90, 0.05)$. The resulting loss of amplitude is greater than the loss shown in Figure 7, for the time interval shown.

Because of the sawtooth computational mode that is allowed by the leapfrog scheme, an Asselin filter (e.g., Durran [6]) is applied at each time step. For a quantity ϕ, this filter has the form $\bar{\phi}^n := \gamma\phi^{n+1} + (1-2\gamma)\phi^n + \gamma\bar{\phi}^{n-1}$, where γ is a positive constant, and $\bar{\phi}$ is a filtered version of ϕ. This formula represents an adjustment to ϕ^n that is performed immediately after ϕ^{n+1} is computed.

Figure 8 shows the results obtained for the first internal mode with the leapfrog version of the code. In this case the baroclinic time increment is $\Delta t = 600$ sec instead of 1200 sec, due to the more restrictive timestep limitation for the leapfrog method. (See Section 2.2 of [10].) In the present computation $\gamma = 0.05$, so the Asselin filter represents a weighted average with coefficients $(0.05, 0.90, 0.05)$. The noisy behavior at the beginning of the time interval is due to the computational mode, which is excited by the forward step that is used during the initialization for the leapfrog method. Such behavior has also been encountered in the initialization of weather forecast models that use the leapfrog method (Rainer Bleck, personal communication). The Asselin filter successfully eliminates the noise, but the subsequent solution displays a reduced amplitude. Over the 1000-day time interval shown in the figure, the loss of amplitude is more substantial than the decay shown in Figure 7. An additional computation (not plotted here) was performed with $\gamma = 0.125$, so that the weight coefficients in the Asselin filter are $(0.125, 0.75, 0.125)$. With this stronger filter, the noise is removed more quickly, but the amplitude of the smooth solution for large t is very similar to that shown in Figure 8.

5.1.3 First external mode

Figures 9 and 10 show some results obtained for the first external Rossby mode, with the two-level version of the code. Plots of the elevations of the free surface and interface for this mode are given in Figure 4 in Section 4. In the case of Figure 9, the barotropic equations are solved implicitly with the adaptation of the ADI method of Bates [1] mentioned in [10] and in Section 3.3 of the present paper. In this case the time increment for the barotropic subsystem is $\Delta t = 1200$ sec, which is the same as for the baroclinic equations. As indicated by the figure, the computed solution is highly inaccurate. With the present Δt there are 72 baroclinic steps per model day, so the problem is not due to under-resolution in t. Causes for the inaccuracy will not be pursued here. On the other hand, a reasonable solution is obtained when the barotropic equations are solved explicitly with short substeps, as indicated in Figure 10. In this latter case the explicit forward-backward method described in Section 3.3 is used, with 35 barotropic substeps per baroclinic step. The barotropic time increment is then approximately 34.3 seconds. This explicit scheme is used in all of the computations described below.

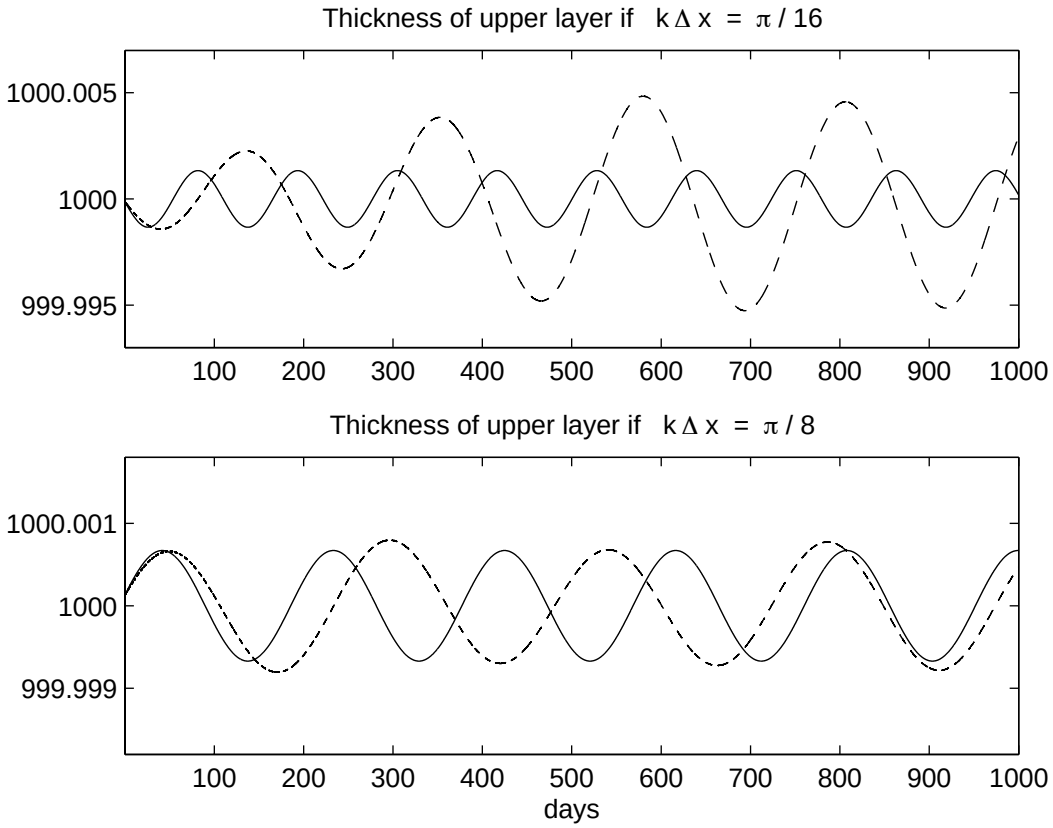

Figure 9: First external Rossby mode. The parameters and format are the same as for Figure 7. The solid curve shows the exact solution, and the dashed curve shows the solution obtained when an alternating-direction implicit method is used to solve the barotropic equations.

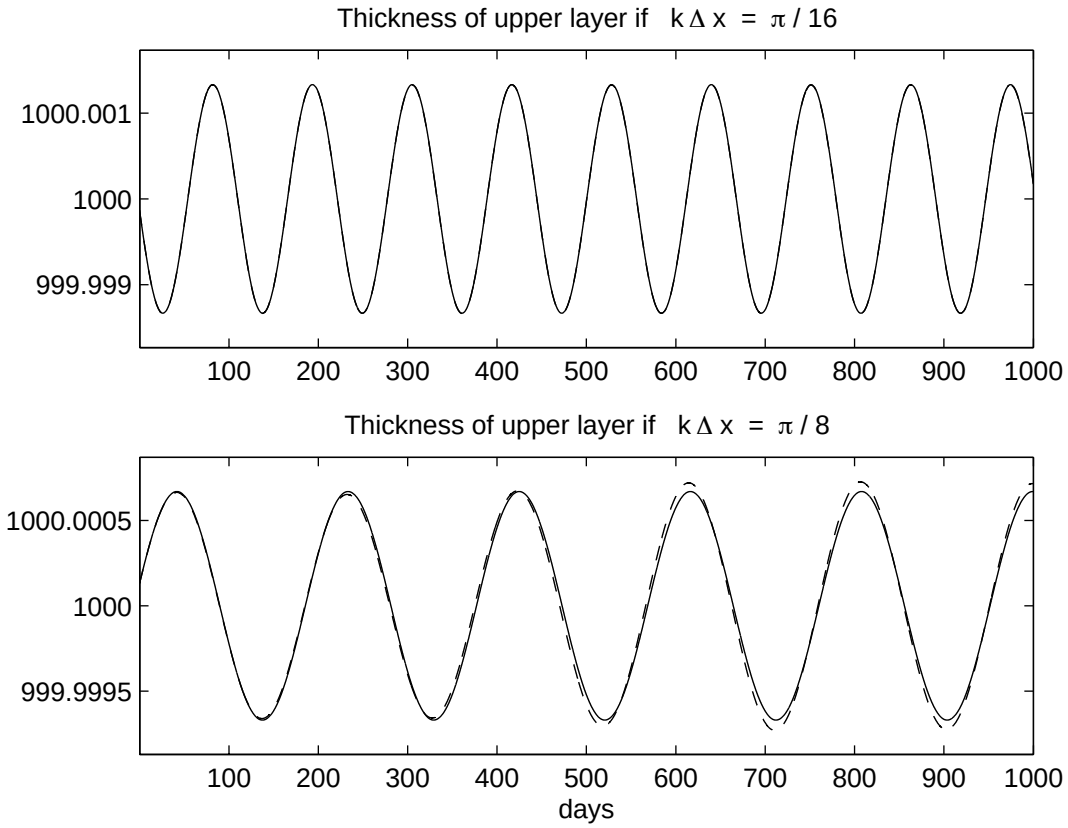

Figure 10: First external Rossby mode, when the barotropic equations are solved with short substeps using the explicit forward-backward method described in Section 3.3. The time interval of 1000 days corresponds to 2.52×10^6 barotropic steps.

An examination of the velocities computed with the solution shown in Figure 10 indicates that the barotropic velocity is typically about three orders of magnitude larger than the baroclinic velocity. Practically all of the energy is represented in the barotropic subsystem, so the present computation provides a test of timestepping methods for that subsystem.

Plots of the thickness of the lower layer (not shown here) indicate that the variations in the thicknesses of the two layers are in phase. In addition, the equilibrium thicknesses of the upper and lower layers are 1000 meters and 3000 meters, respectively, and the amplitude of the perturbation in the upper layer is about one-third the perturbation in the lower layer. This illustrates how layers are thickened or thinned by about the same proportion, in the case of external waves.

5.2 Upwelling and downwelling

In the computations described in the present subsection, the interface between the layers intersects sloping bottom topography, and the thickness of the lower layer tends to zero at such locations. Wind stress is applied at the upper surface of the fluid, and as a consequence the fluid in the upper layer shifts laterally. On a portion of the fluid domain, the lower layer wells upward to the surface, whereas in other locations the upper layer thickens and extends downward. This process is a simple model of upwelling and downwelling phenomena that are found in certain coastal regions.

In the analysis of bottom topography given in Section 4.5 of [10], the goal was to prevent false pressure gradients when layer interfaces intersect the bottom. These procedures were then tested successfully in a problem involving a straight, infinite channel with trapezoidal cross-sections. For some more recent computations described below, this channel is bent into a circle so as to form an annular fluid domain. In this configuration, fluid can flow obliquely to the edges of grid cells, and the fluid in a given layer can flow between adjacent cells having widely varying thicknesses. The concepts of available mass and available momentum described in Section 3.2 were then developed in response to this situation. On the other hand, for the one-dimensional configuration tested in [10], the fluid velocities were essentially parallel to the straight channel. Very little mass was exchanged between adjacent thick and thin cells, so the present difficulty did not arise in that simpler situation.

5.2.1 Straight channel

For completeness, we first repeat the test problem in [10] while using the revised methods for bottom topography. In that configuration, the horizontal coordinates satisfy $0 \leq x \leq 1000$ km, $-\infty < y < \infty$, and the horizontal grid spacing is $\Delta x = \Delta y = 10$ km. Solid boundaries are imposed at $x = 0$ and $x = 1000$ by placing mass cells of zero depth on

each side of the channel. The depth of the fluid is 500 meters for $400 < x < 600$, and elsewhere the bottom undergoes a linear transition to zero depth at the edges. The system is forced by a constant wind stress that has magnitude 0.1 N/m^2 and is directed in the positive y-direction. The Coriolis parameter has a constant value corresponding to 45° N, i.e., $f = 2\Omega \sin 45° \doteq 1.028 \times 10^{-4}$ sec^{-1}, where Ω is the angular rate of rotation of the earth. All aspects of the problem are independent of y, so the solution is independent of y, and the infinite extent in y is simulated with periodic boundary conditions. The timestep used for the baroclinic equations is 2400 sec, and the timestep used for the explicit solution of the barotropic equations is 100 sec.

The upper and lower layers have specific volumes 0.975×10^{-3} m^3/kg and 0.970×10^{-3} m^3/kg, respectively. At the initial time $t = 0$, the free surface is located at $z = 0$ and the interface between the layers is located at $z = -50$ meters. The interface intersects the sloping bottom topography on each side of the channel. Each layer is assumed to exist at all horizontal locations, and at $t = 0$ the lower layer is assigned zero thickness in all mass cells for which only the upper layer is active.

The horizontal viscosity A_H is set to zero. However, the computation employs a nonzero bottom stress and a nonzero shear stress between layers so that the computed solution converges to a steady state that can be compared to an analytical steady state. The bottom stress is taken to be $\tau_{bot} = c_{_D} \rho_2 |\mathbf{u}| \mathbf{u}$, where $c_{_D} = .003$ and $\rho_2 = 1/\alpha_2$. Here, $\mathbf{u}$ represents a value of bottom velocity which is obtained by a mass-weighted vertical average over a prescribed vertical range, which was taken to be 5 meters for the present computations. Also, we use a sign convention that a stress represents a force exerted by an upper region on a lower region. The shear stress at the interface between the layers is represented as

$$\tau_{shear} = \frac{\rho A_V}{\Delta z} \left(\mathbf{u}_1 - \mathbf{u}_2 \right), \tag{44}$$

where $\Delta z = \sqrt{2A_V/f}$ is the Ekman thickness, the vertical viscosity is $A_V = 10^{-4}$ m^2/sec, and $\rho = 1/\alpha_1$. Shear stress is often modeled by the relation $\tau = \rho A_V \partial \mathbf{u}/\partial z$ (Pedlosky [13]), but for a layered model the vertical increments Δz can be highly irregular, and Taylor expansions show that finite difference approximations with irregular values of Δz need not be consistent with the analytical limit. The above representation with constant Δz was used in order to provide some kind of friction so that the solution converges to a steady state for purposes of testing.

When the wind stress is applied at the upper surface, its magnitude decays linearly to zero over a prescribed vertical distance which was taken to be one meter for the present computations. If the thickness of the upper layer exceeds this distance, then the wind stress is applied entirely to the upper layer. However, if the thickness of the upper layer is less

than this threshold, then some of the wind stress is applied directly to lower layers. This procedure prevents large forcing from being applied to arbitrarily thin layers. An analogous procedure is used for the bottom stress.

The system begins in a state of rest. Due to the action of the wind stress and Coriolis effect, the fluid in the upper layer then shifts slowly in the positive x-direction. (Essentially, when the Coriolis parameter is positive, as in the northern hemisphere, fluid shifts to the right when wind stress is applied.) At the left edge of the channel (near $x = 0$) the interface moves upward along the sloping bottom topography; equivalently, some mass in layer 2 moves into cells which were initially massless. At the right edge of the channel (near $x = 1000$) the interface moves downward along the bottom slope, i.e., some cells in layer 2 which initially contain mass are drained and then have thicknesses that are essentially zero. As the fluid builds up on the right side of the domain, a cross-channel pressure gradient is established which begins to balance the Coriolis effect, and as $t \to \infty$ the system approaches a steady state. For sufficiently large t, the entire upper layer has shifted to the right and is confined to a region near the right edge of the channel.

A steady-state analytical solution to this problem was derived in [10]. In regions where only one layer has positive thickness, the wind stress at the upper boundary is balanced by bottom stress at the lower boundary. The bottom stress depends on velocity, so this balance determines the velocity in the active layer. The velocity in the inactive layer is assumed to be the same as in the active layer, in keeping with the action of the shear stress as described in Section 3.1 of the present paper. The velocity, coupled with the geostrophic balance between the Coriolis terms and pressure gradient, then determines the slope of the free surface. In regions where both layers are active, the wind stress, shear stress, and bottom stress are all equal. This balance implies that the velocity in the lower layer is determined by the wind stress. The upper layer can slide over the lower layer, so the velocity in the upper layer displays a jump discontinuity at locations where the number of active layers changes. At locations where two layers are active, the free surface is steeper than elsewhere, due to the larger velocity and the geostrophic balance.

In the present computation, the solution is essentially at a steady state by day 1200, and the solution at that time is shown in Figure 11. In the bottom frame in the figure, the y-component of the velocity in the upper layer agrees very closely with the values obtained in the analytical steady state. The jump discontinuity in v then generates a jump discontinuity in the slope of the free surface, which is illustrated in the middle frame. The slopes of the free surface, and the slope of the interface in the top frame, were calculated in [10] for the analytical steady state. An inspection of numerical output (not shown here) indicates that the computed slopes agree with the analytical values to two or three significant digits.

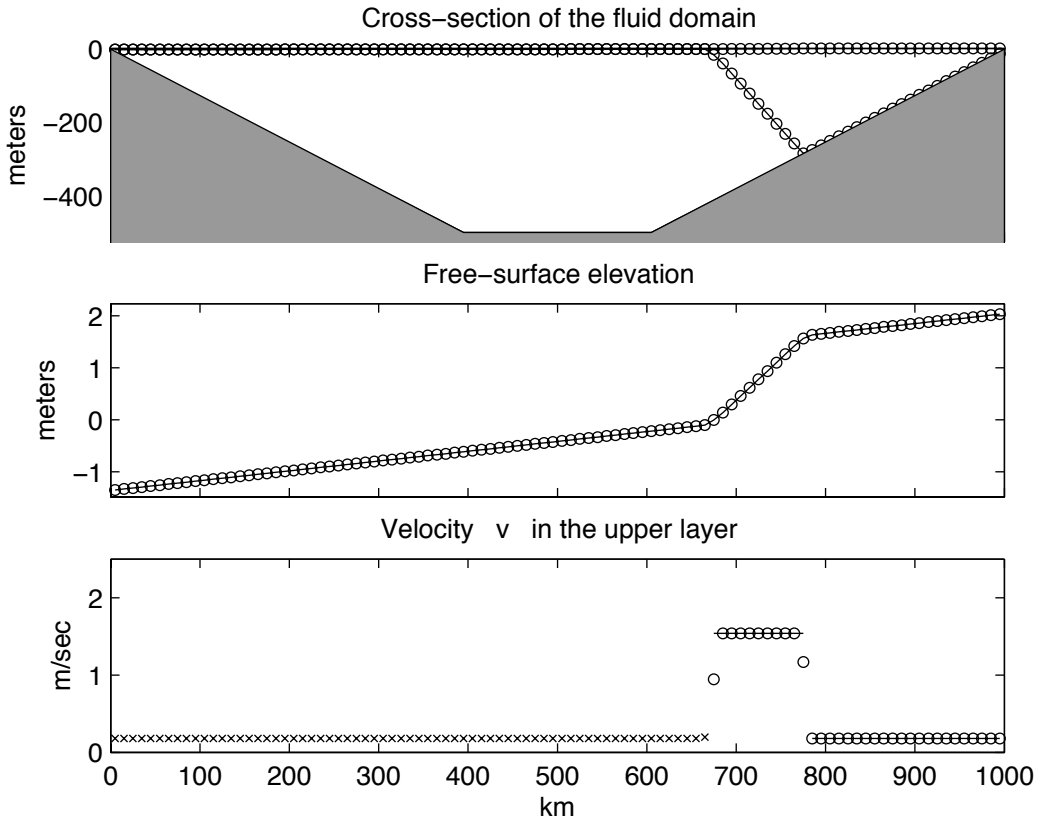

Figure 11: Upwelling and downwelling in a straight channel. The solution is shown at day 1200, when the system is essentially at a steady state. All aspects of the problem are independent of the along-channel direction y, so the solution is also independent of y. In each frame, each symbol (circle or $\times$) represents a value of the numerical solution at a single grid point. The top frame illustrates a cross-section of the fluid domain for fixed y. The free surface is located at $z \approx 0$, the upper layer is confined to the triangular region in the upper right, and the shaded region represents bottom topography. The middle frame shows the elevation of the free surface. The bottom frame shows the along-channel velocity v in the upper layer. In that frame the solid horizontal lines for $x > 680$ represent values of v in the analytical steady-state solution. The $\times$ symbols indicate values of v at locations where the upper layer is essentially massless; at such locations the velocity is essentially the same as in the lower layer, due to the effect of shear stress between layers.

5.2.2 Circular channel

Next consider the case where a trapezoidal channel is bent into a circle to form an annular fluid domain. Consider a square region that is discretized with 128 mass cells in the x-direction and 128 mass cells in the y-direction, with $\Delta x = \Delta y = 10$ km, and let (x_0, y_0) denote the center of that region. For each mass cell, let r denote the distance from (x_0, y_0) to the center of that cell. Assume that the depth of the fluid in a cell is nonzero if and only if $r_1 < r < r_2$, where r_1 and r_2 are positive constants. Also assume that $r_1 = r_2/4$ and that the inner sloping side, outer sloping side, and level bottom each occupy one-third of the radial interval $[r_1, r_2]$. In the following, r_2 is Δx less than half the side of the square.

The layer densities, initial layer thicknesses, Coriolis parameter, baroclinic timestep, and barotropic timestep are the same as in the case of the straight channel described above. The shear stress between layers has the same form as above, but with $A_V = .0005$. The system is forced by a tangential wind stress that points counter-clockwise along the length of the channel. The wind stress is constant in t and is directly proportional to the radius r, with a magnitude of $\tau_{max} = 0.1$ N/m^2 at the outer radius $r = r_2$.

For the present computation, the bottom stress is represented as $\tau_{bot} = c_{_D} \rho_2 \mathbf{u}$, where $c_{_D} = .0005$, instead of the quadratic form used above. In situations where the tangential velocity is determined by a balance between wind stress and bottom stress, the bottom stress is proportional to r since the wind stress is proportional to r. If the bottom stress is proportional to tangential velocity, then this velocity is also proportional to r. The resulting rigid-body rotation is a convenient formulation for an analytical steady state. As in the preceding test, the bottom stress and wind stress decay linearly to zero over a vertical range of one meter.

We next derive the analytical steady state. At any point in the channel, let u_k and v_k denote the radial (cross-channel) and tangential (along-channel) components of velocity, respectively, in layer k for $k = 1, 2$. The momentum equations can then be written in the polar form

$$\begin{aligned} \frac{Du_k}{Dt} - \frac{v_k^2}{r} - f v_k &= -\frac{\partial M_k}{\partial r} + \frac{g \Delta \tau_k^r}{\Delta p_k} \\ \frac{Dv_k}{Dt} + \frac{u_k v_k}{r} + f u_k &= -\frac{1}{r}\frac{\partial M_k}{\partial \theta} + \frac{g \Delta \tau_k^\theta}{\Delta p_k}, \end{aligned} \tag{45}$$

where D/Dt denotes the material derivative, and $\Delta \tau_k^r = \tau_{k-1/2}^r - \tau_{k+1/2}^r$ and $\Delta \tau_k^\theta = \tau_{k-1/2}^\theta - \tau_{k+1/2}^\theta$ are the radial and tangential components, respectively, of the vertical stress difference across layer k. Now suppose that the system is at a steady state for which each fluid parcel moves at a uniform speed in a circle centered about $r = 0$ and for which the layer thicknesses are independent of the angle θ. The first assumption implies $u_k = 0$ and $Dv_k/Dt = 0$, and

the tangential directions of the wind, shear, and bottom stresses imply $\Delta\tau_k^r = 0$. The system (45) then simplifies to

$$-\frac{v_k^2}{r} - fv_k = -\frac{\partial M_k}{\partial r} \tag{46}$$

$$\Delta\tau_k^\theta = 0. \tag{47}$$

The quantity v_k^2/r is the centripetal acceleration, and in the case $f = 0$ the free surface and the layer interface vary with r so that $\partial M_k/\partial r$ provides the required acceleration. In the present situation the tangential components of the wind, shear, and bottom stresses are given by $\tau_{wind} = \tau_{max}(r/r_2)$,

$$\tau_{shear} = \frac{\rho_1 A_V}{\Delta z}(v_1 - v_2), \tag{48}$$

and $\tau_{bot} = c_{_D}\rho_2 v_2$, respectively. Here, $\Delta z = \sqrt{2A_V/f}$, as in (44).

Consider a region where only one layer has positive thickness, and denote this layer with index k. In this case $\tau_{k-1/2}^\theta = \tau_{wind}$ and $\tau_{k+1/2}^\theta = \tau_{bot}$, and equation (47) then implies $\tau_{bot} = \tau_{wind}$. As before, assume $v_1 = v_2$ in locations where one layer vanishes. We then have

$$v_1 = v_2 = \left(\frac{\tau_{max}}{\rho_2 c_{_D} r_2}\right) r. \tag{49}$$

Now let z_{top} denote the elevation of the free surface at the top of the fluid. If layer 1 is the active layer, then $M_k = M_1 = \alpha_1 p_{top} + g z_{top} = g z_{top}$. (Here, we assume $p_{top} = 0$.) If layer 2 is the active layer, then $M_2 = M_1 - p_{top}(\alpha_1 - \alpha_2) = M_1 = g z_{top}$. In either case, we have $M_k = g z_{top}$. Equations (46) and (49) then imply

$$\frac{\partial z_{top}}{\partial r} = \frac{1}{g}\frac{\partial M_k}{\partial r} = \frac{\gamma}{g}(f + \gamma)r, \tag{50}$$

where $\gamma = \tau_{max}/(\rho_2 c_{_D} r_2)$. The elevation z_{top} then varies quadratically with the radius r.

If both layers have positive thickness, then $\tau_{wind} = \tau_{shear} = \tau_{bot}$. Since $\tau_{wind} = \tau_{bot}$, it follows that v_2 has the value given in (49). Equation (48) for the shear stress, together with $\tau_{shear} = \tau_{wind}$, implies

$$v_1 = v_2 + \frac{\Delta z}{\rho_1 A_V}\tau_{wind} = \tau_{max}\left[\frac{1}{\rho_2 c_{_D}} + \frac{\Delta z}{\rho_1 A_V}\right]\frac{r}{r_2} \tag{51}$$

for the case of two active layers. The velocities v_1 and v_2 are each proportional to r, so the momentum equation (46) implies that M_1 and M_2 are each quadratic in r. It then follows that the elevations of the free surface and layer interface are also quadratic in r.

The value of v_1 in (51) is greater than the value of v_1 given in (49) for the case of one active layer. The expression (46) for $\partial M_k/\partial r$ then implies that the free surface varies more rapidly with r when there are two active layers than when there is one active layer.

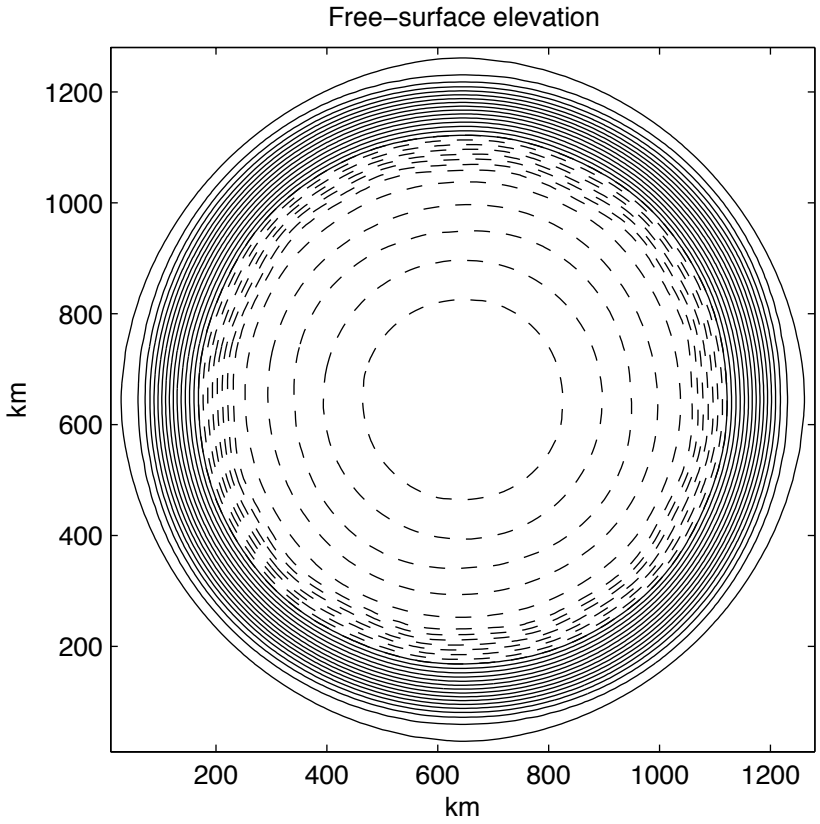

Figure 12: Upwelling and downwelling in a circular channel. The fluid occupies an annular region having trapezoidal vertical cross-sections. This figure shows a contour plot of the free surface elevation at day 400, with a contour interval of 5 centimeters. Solid curves show positive elevation relative to the equilibrium state, and dashed curves show negative elevation relative to that state.

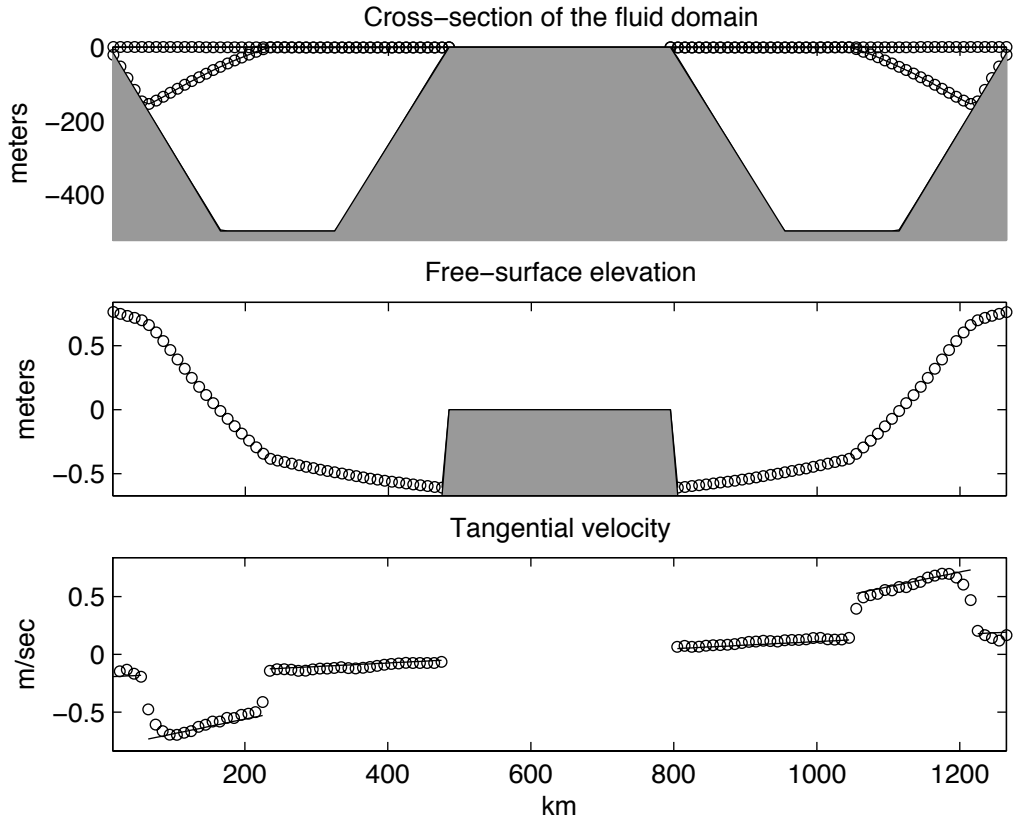

Figure 13: Upwelling and downwelling in a circular channel. These plots show cross-sections through the center for fixed y at day 400. The shaded regions represent bottom topography. In the bottom frame, the solid line segments represent values of tangential velocity in the upper layer in the analytical steady state, and the circles represent computed values. The fluid flows counter-clockwise in the annular domain, so on the right side the velocity is into the page, whereas on the left side the velocity is out of the page.

For the present computation, the system begins at rest, and the steady wind stress is applied for $t > 0$. Because of the action of the wind stress and the Coriolis effect, the fluid in the upper layer shifts towards the outer edge of the annular domain, and the fluid in the lower layer wells upward along the inner edge.

Figure 12 shows a contour plot of the elevation of the free surface at day 400. The figure indicates that the computed solution is very nearly radially symmetric. Figure 13 shows cross-sections of the solution for fixed y through the center of the domain, also at day 400. The top frame in that figure illustrates how the fluid in the upper layer has migrated to the outer rim of the fluid domain. The middle figure shows the elevation of free surface, and in particular it illustrates how the free surface is steeper in locations where both layers have positive thickness. The bottom frame indicates that the computed values of velocity agree closely with the values obtained in the analytical steady state.

The computation was continued past day 400 to day 2000. Over this time period the solutions (not shown here) remain similar to the solution shown in Figures 12 and 13, except that a wavy pattern appears in the contours of the free-surface elevations. These waves are visible by day 600 and maintain nearly the same amplitude through day 2000. The waves are confined to the contours slightly below zero elevation. At day 600 there are twelve wavelengths per contour, and by day 1000 there are eight wavelengths per contour. These wavelengths are far longer than the grid scale, so apparently they are a result of hydrodynamic instability instead of any kind of numerical instability.

In this computation the barotropic equations are solved explicitly with the forward-backward method described in Section 3.3. The computation was repeated, but while solving the barotropic equations with the ADI method discussed in that section. With the ADI method, the wavy patterns do not appear, but instead the numerical solution remains at a steady state that agrees closely with the analytical steady state. However, the validity of the ADI solution is questionable because of the experience with Rossby waves described in Section 5.1.

5.3 Double gyre

The present subsection describes a test in which a spatially-varying wind stress generates a double-gyre circulation in a square basin with a flat bottom. In this case the computed solutions will not be compared with an analytical solution, but instead the discussion of results is qualitative. In particular, the flow displays numerous meanders and eddies, which are prominent features in the circulation of the real ocean. The previous test problems are too constrained to allow meanders and eddies, and part of the purpose of the present test is to demonstrate the ability of the model to represent such features. In addition, the lower

layer wells up to the surface on a portion of the domain.

The computational domain consists of 200 mass cells by 200 mass cells, with a uniform grid spacing of $\Delta x = \Delta y = 10$ km. Along the boundary the outermost row of mass cells has zero depth, so the fluid domain has dimensions 1980 km $\times$ 1980 km. Initially the upper and lower layers have thicknesses 100 meters and 900 meters, respectively, and the specific volumes of these layers are 0.976×10^{-3} m^3/kg and 0.972×10^{-3} m^3/kg. Regard the positive x-axis and positive y-axis as eastward and northward, respectively, and denote the extent of the domain in the y-direction by $[y_0 - L, y_0 + L]$. For purposes of the present test, represent the Coriolis parameter with the linear beta-plane approximation $f = f_0 + \beta(y - y_0)$, where f_0 and β are the values of f and $\partial f/\partial y$ at 45° N.

The baroclinic time increment is $\Delta t = 2400$ sec. The barotropic equations are solved with the explicit method described in Section 3.3, with a nominal barotropic time increment of 70 sec. There are then 35 barotropic substeps per baroclinic step. The horizontal viscosity is $A_H = 0$, except for the computation illustrated in Figure 18. The bottom stress and the shear stress between layers are implemented in the same manner as in Section 5.2. The former uses the quadratic version $\tau_{bot} = c_{_D} \rho_2 |\mathbf{u}|\mathbf{u}$, with $c_{_D} = .003$.

The system is forced at the upper surface by a steady wind stress $\tau = (\tau_x, \tau_y)$ for which $\tau_y = 0$ and $\tau_x = \tau_{max} \cos[\frac{\pi}{L}(y - y_0)]$, where $\tau_{max} = 0.1$ N/m^2. The wind stress points eastward in the middle of the domain and westward near the northern and southern boundaries. The wind stress decays linearly to zero over a vertical range of one meter, as in Section 5.2.

Because of the action of the wind stress and the Coriolis effect, the flow develops two closed loops (gyres). In the northern gyre the flow is counterclockwise, and in the southern gyre the flow is clockwise. In addition, the fluid in the upper layer shifts southward, so that the free surface becomes elevated in the southern gyre and depressed in the northern gyre. This is illustrated in Figure 14, which shows the solution after 25 days. The system is near a state of geostrophic balance between the Coriolis and pressure terms, i.e., $(-fv_r, fu_r) \approx -\nabla M_r$ in layer r. But $M_1 = gz_{top}$, so the velocity (u_1, v_1) in the upper layer is tangent to curves of constant elevation of the free surface. The curves in Figure 14 can then be regarded as streamlines for the flow in the upper layer.

As t increases the flow becomes more complex. By about day 500 (not shown here) the thickness of the upper layer is near zero in a small portion of the northern half of the domain, due to the continued southward shift of the fluid in the upper layer, and by day 600 meanders and eddies have begun to appear in the west-to-east jet in the middle of the domain and in the currents along the northern and southern boundaries. As t increases further the details of the flow continue to vary, but the general pattern remains similar. For example, the elevation of the free surface at day 1500 is shown in Figure 15. The meanders in the flow are evident,

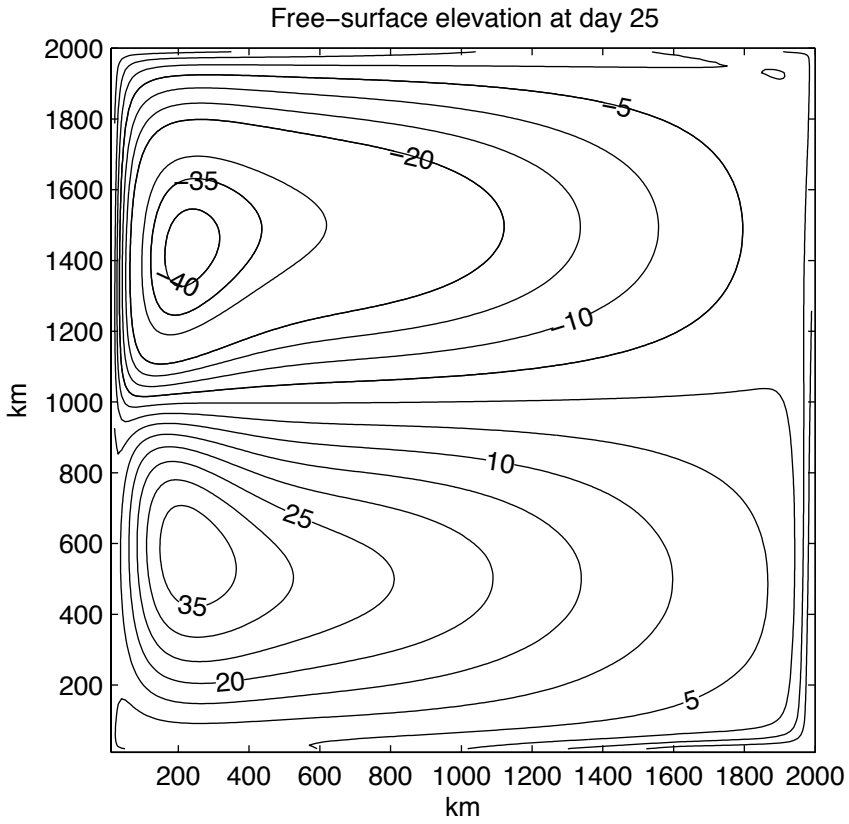

Figure 14: Double-gyre experiment. This figure shows a contour plot of the elevation of the free surface at day 25, with a contour interval of 5 centimeters. The elevation is positive in the southern half of the domain and negative in the northern half. The contours can be regarded as streamlines for the flow in the upper layer. In the middle of the domain the fluid flows eastward, and it then separates to the north and south and completes the loops via western boundary currents.

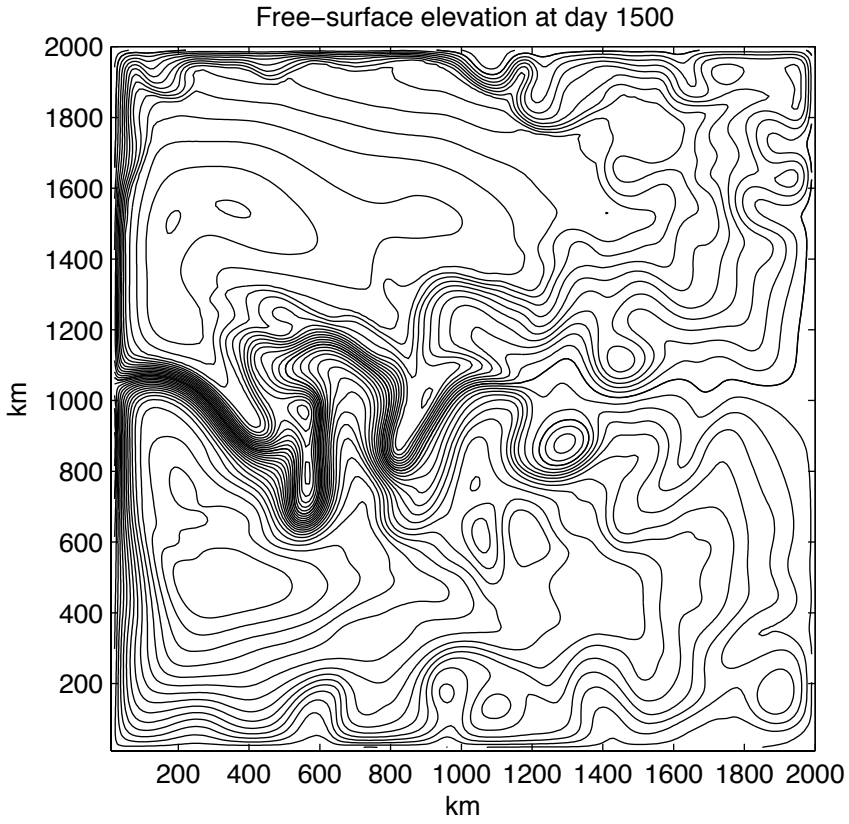

Figure 15: Contour plot of the free-surface elevation at day 1500. The contour interval is 5 centimeters, with lower elevations in the northern region and higher elevations in the southern region. The maximum and minimum elevations are approximately 85 cm and -71 cm, respectively.

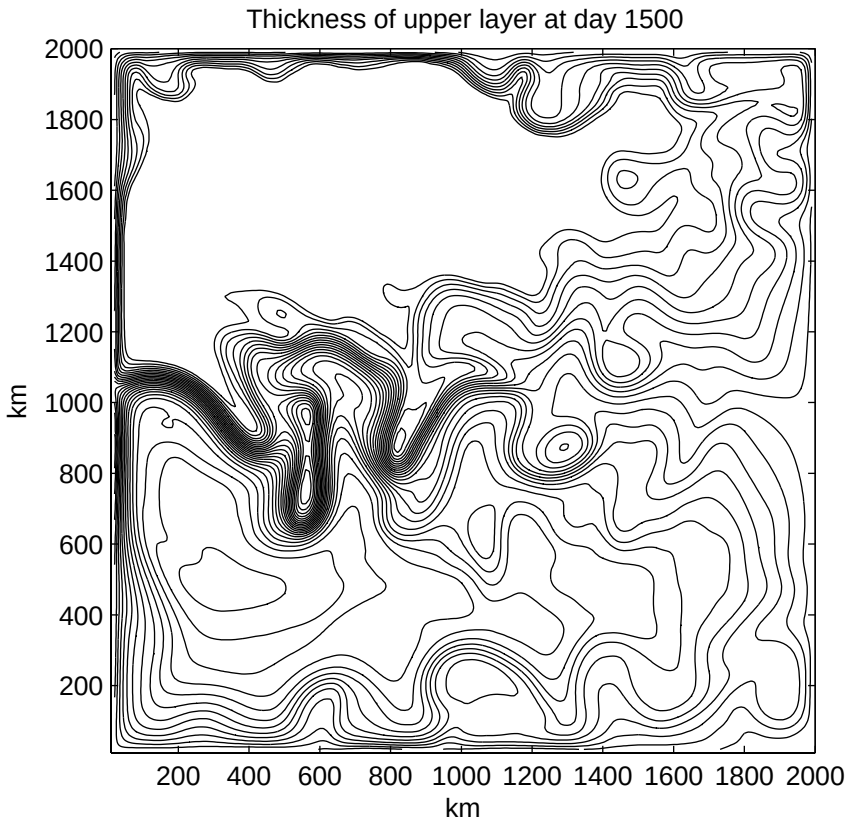

Figure 16: Contour plot of the thickness of the upper layer at day 1500. The contour interval is 10 meters. Over much of the northern region the lower layer wells up to the surface, so the thickness of the upper layer is near zero in such locations. The maximum and minimum computed thicknesses for the upper layer are approximately 244 and 10^{-9} meters, respectively.

and various eddies can be recognized by relatively small closed loops in the contours. The free surface is still elevated in the southern region and depressed in the northern region, and the flow still follows the general pattern of clockwise circulation in the southern gyre and counter-clockwise circulation in the northern gyre. The flow along the western boundary consists of intense northward and southward boundary currents which meet in the middle, and the maximum velocity in these western boundary currents is approximately 1.5 m/sec.

The thickness of the upper layer at day 1500 is shown in Figure 16, which indicates that the lower layer has welled up to the surface over much of the northern half of the domain. An inspection of numerical output (not shown here) indicates that for many mass cells the thickness of the upper layer is on the order of centimeters or millimeters, and the minimum computed thickness of the upper layer is approximately 10^{-9} meters.

Figure 17 shows a close-up view of the flow at day 1500 in a region to the west of the center

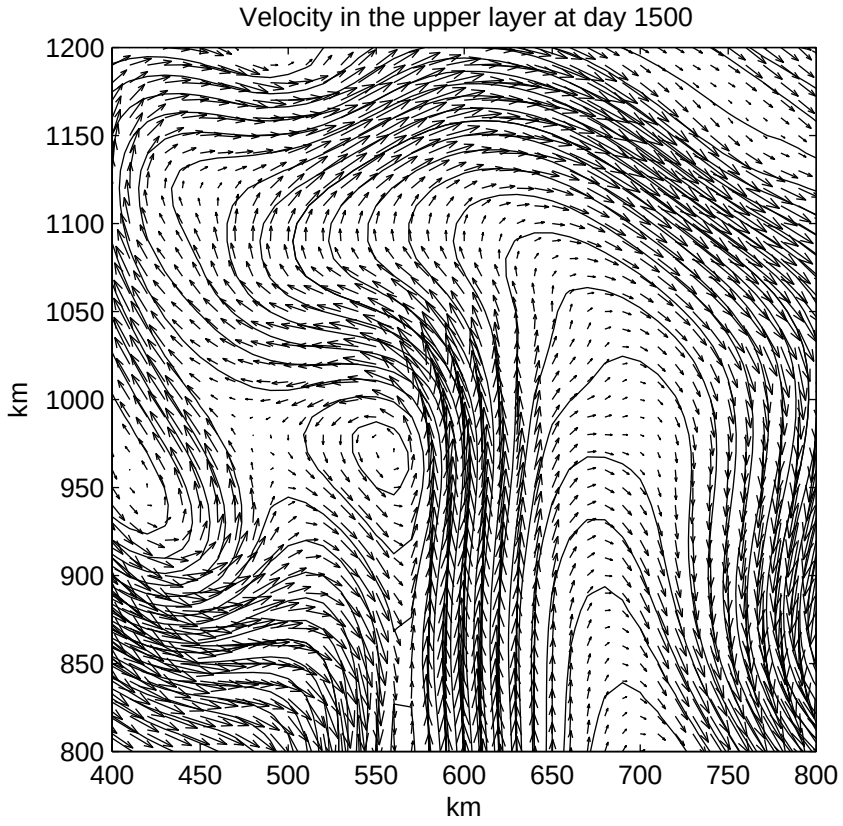

Figure 17: Close-up view of the velocity field in the upper layer at day 1500, together with contours of the elevation of the free surface. This plot shows a subregion to the west of the center of the fluid domain, where the west-to-east jet is relatively active. Velocity vectors are shown at every grid point, and the contour interval for the free surface is 5 centimeters.

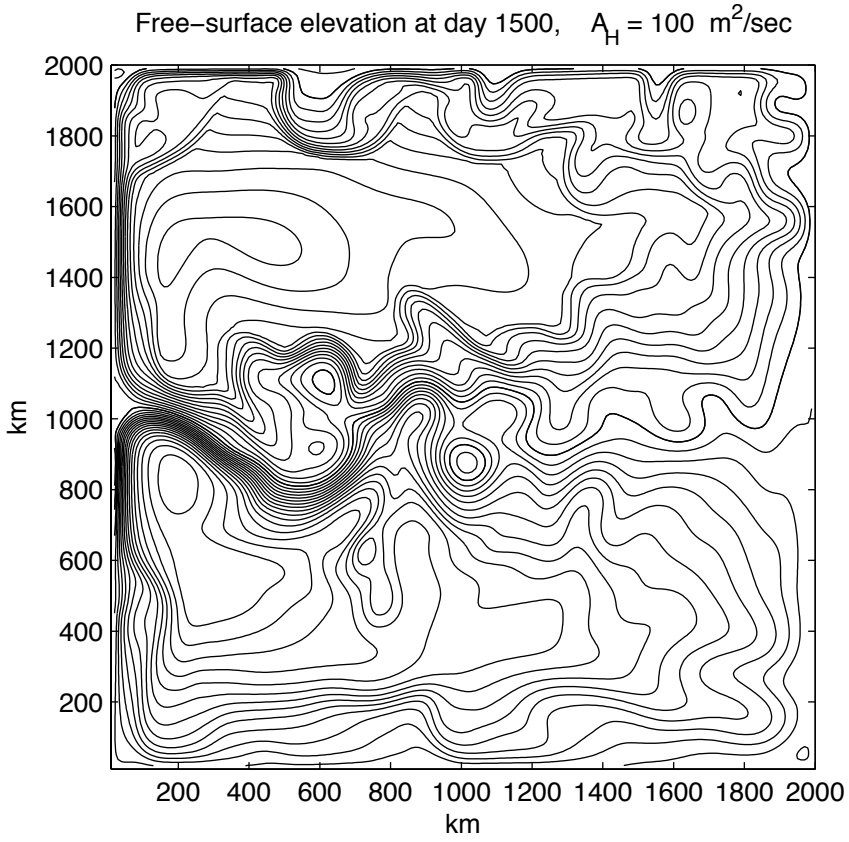

Figure 18: Contour plot of the free-surface elevation at day 1500, when the horizontal viscosity is $A_H = 100$ m^2/sec. For the preceding plots this viscosity is zero.

of the fluid domain, where the west-to-east jet is relatively active. The curves are contours of the free-surface elevation, and the arrows represent velocity vectors. The alignment of the velocity vectors with the contours illustrates the geostrophic balance in the flow. The velocity vectors are shown at every grid point, or more precisely, for each mass cell the value of u on the western edge and the value of v on the southern edge are combined into a vector (u, v) that is located at the center of the mass cell. A slightly more realistic velocity field would be obtained with averages of u and v across the cell. However, such averaging would obscure any grid noise that might be present, whereas the vector field shown in Figure 17 indicates that grid noise is not present to a perceptible degree.

A plot of the velocity field in the lower layer (not shown here) indicates that the flow patterns in the two layers share some features, but they are not the same. For example, a small eddy has developed to the left of the center of Figure 17, and this eddy is confined to the upper layer.

As an experiment, the preceding computation was repeated with a nonzero value of the

horizontal viscosity given by $A_H = 100$ m^2/sec. All other aspects of the model were the same as in the preceding computation. The elevation of the free surface for this run is shown in Figure 18. Compared to the solution shown in Figure 15, the west-to-east jet is less active, the western boundary layer is thicker, and the flows along the northern and southern boundaries are less intense, as expected. The insertion of horizontal viscosity also causes a slight shift in the location where the western boundary currents separate from that boundary; in operational situations, ocean modelers sometimes tune the value of viscosity to adjust the locations where such separation takes place.

The preceding computation was also performed with the leapfrog version of the code that is described in Section 5.1.2. In this version, the bottom, shear, and wind stresses are represented in the same manner as in the two-level code used in the computations discussed above. For the Asselin filter that is used to suppress the sawtooth computational mode in t, the smoothing parameter is $\gamma = 0.125$, so the Asselin filter involves a weighted average with coefficients $(0.125, 0.75, 0.125)$. In addition, the horizontal viscosity is set to the value $A_H = 100$ m^2/sec. For a few hundred model days, the code produced reasonable results, but the computation crashed at about day 503. The instability was first manifested in regions where a layer thickness is near zero and a strong horizontal shear is present. It might be possible to mitigate the problems by stronger regularization procedures, such as increasing the vertical distances over which the wind stress and bottom stress decay to zero, but these options were not pursued here. The problems are perhaps related to the computational mode in t and/or oscillatory behavior allowed by centered spatial differencing of the nonlinear and vorticity terms. These issues are avoided by the algorithms that have been discussed in the present paper.

6 Summary

The purpose of this paper is to describe some further developments related to the implementation and testing of the two-level time-stepping method developed in [10].

One such step is the formulation of a test problem involving a two-layer fluid in a channel. This system admits both gravity waves and Rossby waves, and within each class the system admits both external and internal waves. The separation into external and internal modes makes it possible to test the time-stepping methods for the barotropic and baroclinic subsystems independently. Here, the emphasis is on Rossby waves, as a simpler test problem involving gravity waves was already described in [10]. The present analysis yields exact solutions, up to the numerical accuracy in computing eigenvalues and eigenvectors of certain matrices.

The algorithmic developments include the following.

(1) The baroclinic velocity must be extracted from the baroclinic momentum density, for the sake of computing fluxes of mass and momentum. Here, well-behaved velocities are obtained with a procedure that involves the shear stress between layers and the implicit implementation of the Coriolis terms with the velocity form, not momentum form, of the baroclinic momentum equation. The final values of baroclinic momentum density are then constructed with a multiplication.

(2) In regions where layer interfaces intersect variable bottom topography, a given layer can have widely varying thicknesses in adjacent mass or momentum cells. In order to prevent unrealistically large transports of mass or momentum from thick cells into adjacent thin cells, we use the concepts of "available mass" and "available momentum" when computing mass and momentum fluxes. These quantities are defined in terms of the portion of a layer, in a given cell, that lies above the stairstep bottom topography.

(3) The barotropic (fast) subsystem can be solved implicitly with long time steps or explicitly with many short substeps. In a test problem involving an external Rossby wave, an alternating-direction implicit method gives inaccurate results, whereas good results are obtained with an explicit scheme. With the explicit scheme, a simple second-order time average is used near the beginning of each (long) baroclinic time interval in order to eliminate numerical noise caused by a slight discontinuity in forcing between consecutive baroclinic intervals.

(4) The baroclinic mass equation of [3] does not yield exact conservation of mass in individual layers. Exact conservation can be obtained with the unsplit mass equation, and stable behavior can be obtained by enforcing a kind of consistency between the layer mass equations and the barotropic (vertically-summed) mass equation. Related ideas have been used elsewhere; the present version involves an upwind formulation of flux adjustments and the concept of available mass.

The two-level method, with associated algorithms, gives good results in some numerical experiments involving Rossby waves, variable bottom topography, and a double-gyre circulation that displays meanders and eddies. In particular, the method avoids the disadvantages of the computational mode that is allowed by the traditional leapfrog method, and when the explicit viscosity is set to zero the model behaves stably and does not display grid noise.

7 Acknowledgments

I thank John Baumgardner, Mats Bentsen, Rainer Bleck, Roland de Szoeke, John Dukowicz, Robert Miller, and Scott Springer for useful conversations on various matters related to the

contents of this paper. In particular, Bentsen pointed out the idea of requiring that the vertical sum of the mass fluxes in individual layers be equal to the mass flux used in the barotropic subsystem. This work was supported by National Science Foundation grant DMS-0107495.

References

[1] J. R. Bates, An efficient semi-Lagrangian and alternating direction implicit method for integrating the shallow water equations, *Monthly Weather Rev.* **112**, 2033 (1984).

[2] R. Bleck, An oceanic general circulation model framed in hybrid isopycnic-Cartesian coordinates, *Ocean Modelling*, **4**, 55 (2002).

[3] R. Bleck and L. T. Smith, A wind-driven isopycnic coordinate model of the north and equatorial Atlantic Ocean 1. Model development and supporting experiments, *J. Geophys. Res.* **95C**, 3273 (1990).

[4] R. A. de Szoeke and S. R. Springer, A diapycnal diffusion algorithm for isopycnal ocean circulation models with special application to mixed layers, *Ocean Modelling* **5**, 297 (2003).

[5] J. K. Dukowicz, *HYPOP Summary (Hybrid vertical coordinate version of POP) Current C-Grid Version*, Technical Report LA-UR-04-8586, Los Alamos National Laboratory, 2004 (unpublished).

[6] D. R. Durran, *Numerical Methods for Wave Equations in Geophysical Fluid Dynamics* (Springer, New York, 1999).

[7] A. E. Gill, *Atmosphere-Ocean Dynamics* (Academic Press, San Diego, 1982).

[8] R. Hallberg, Stable split time stepping schemes for large-scale ocean modeling, *J. Comput. Phys.* **135**, 54 (1997), doi:10.1006/jcph.1997.5734.

[9] R. L. Higdon, Implementation of a barotropic-baroclinic time splitting for isopycnic coordinate ocean modeling, *J. Comput. Phys.* **148**, 579 (1999), doi:10.1006/jcph.1998.6130.

[10] R. L. Higdon, A two-level time-stepping method for layered ocean circulation models, *J. Comput. Phys.* **177**, 59 (2002), doi:10.1006/jcph.2002.7003.

[11] R. L. Higdon and R. A. de Szoeke, Barotropic-baroclinic time splitting for ocean circulation modeling, *J. Comput. Phys.* **135**, 30 (1997), doi:10.1006/jcph.1997.5733.

[12] D. M. Holland and A. Jenkins, Adaptation of an isopycnic coordinate ocean model for the study of circulation beneath ice shelves, *Monthly Weather Rev.* **129**, 1905 (2001).

[13] J. Pedlosky, *Geophysical Fluid Dynamics*, 2nd ed. (Springer-Verlag, New York, 1987).

[14] J. Pedlosky, *Waves in the Ocean and Atmosphere* (Springer-Verlag, Berlin, 2003).

[15] R. Sadourny, The dynamics of finite-difference models of the shallow-water equations, *J. Atmos. Sci.* **32**, 680 (1975).

[16] C. Schär and P. K. Smolarkiewicz, A synchronous and iterative flux-correction formalism for coupled transport equations, *J. Comput. Phys.* **128**, 101 (1996).

[17] P. K. Smolarkiewicz and L. G. Margolin, MPDATA: A finite-difference solver for geophysical flows, *J. Comput. Phys.* **140**, 459 (1998), doi:10.1006/jcph.1998.5901.

[18] G. Strang, On the construction and comparison of difference schemes, *SIAM J. Numer. Anal.* **5**, 506 (1968).